

Stratospheric Sulfate Aerosol Injection as a Climate Change Mitigation Strategy: Effectiveness and Feasibility

by

Bethan Cordone

A Thesis submitted to the Faculty

in partial fulfillment of the requirements for the

BACHELOR OF ARTS

Accepted

Dr. Michael Bergman, Thesis Advisor

Dr. Eric Kramer, Second Reader

John B. Weinstein, Provost and Vice President

Bard College at Simon's Rock
Great Barrington, Massachusetts

May 2022

Acknowledgements

I would like to thank my family, advisors, and friends for their help and support throughout the thesis process and my academic journey. To my parents (Pete and Wiley) for nurturing my passions and supporting my academic journey at Bard College at Simon's Rock and Columbia University. To my partner, Finlay Stenton, for his assistance in editing and the emotional support he provided throughout the thesis process. To my suitemates and friends, thanks for the laughs, it was a much needed break. Finally, to Dr. Mike Bergman and Dr. Eric Kramer for their mentorship and support as advisors. I dedicate this thesis to the person I was at 16 when I left home for the unknown. I wouldn't be where I am today without you.

Table of Contents

Introduction	5
Part 1: Background Information	4
Chapter 1: Aerosols in the Atmosphere	4
Section 1: Categorization of aerosols	5
Section 2: Aerosol Patterns	7
Section 3: Direct and Indirect Effects	11
Section 4: Measurement of Aerosols	16
Chapter 2: Natural Evidence for Aerosol Atmospheric Cooling	19
Section 1: The Little Ice Age	20
Section 2: Major Radiative Processes of Major Volcanic Eruptions	26
Section 3: Major Volcanic Eruptions into the Stratosphere	29
Section 4: Weather and Climate Response	32
PART 2: The Model Comparison	37
Chapter 3: Model Descriptions	37
Section 1: The Geoengineering Intercomparison Project (GeoMIP)	37
Section 2: The Climate Models Used	43
Section 3: The RCR Method (Residual Climate Response)	45
Chapter 4: Procedure	49
Section 1: NCAR Datasets	49
Section 2: Area Weighted Global Mean Calculation	51
Section 3: Global Anomalies Graphs and Coordinate Transformation	52
Section 4: Regional Area Weighted Averages	54
Chapter 5: Results and Discussion	59
Section 1: Global Area Weighted Mean Results	59
Section 2: Regional Area Weighted Mean Results	61
Section 3: Grid Level Map Outputs	77
Conclusions	86
Bibliography	88

Abstract

This thesis explores the effectiveness of aerosol injection as a climate change mitigation strategy through the comparison of different models. It explores the general workings of aerosols as well as the climatic effects of volcanic eruptions into the stratosphere. Volcanic eruption data indicates that sulfate aerosols in the stratosphere decrease temperatures globally with a greater impact on the Northern Hemisphere. The paper *Impacts, effectiveness and regional inequalities of the GeoMIP G1 to G4 solar radiation management scenarios* (Yu et al., 2015) compares the surface air temperature and precipitation changes for different models using the GeoMIP experiment setup. The GeoMIP experiment design creates a standard for geoengineering modeling experiments so that the results can be easily compared with other models.

The National Center for Atmospheric Research (NCAR) has a database containing model CCSM4 outputs for GeoMIP experiments G1, G2 and G3S. I compared the surface air temperature and precipitation changes between the climate change and reference climate scenarios from the paper and the NCAR outputs on the global, regional, and grid level. On the global scale, the models agree and show that aerosols are effective in counteracting increased radiative forcing due to increased CO₂ concentrations. There is some agreement in results on the regional scale between models but there are many inconsistencies. There are also inconsistencies at the grid level. The analysis concludes that although the evidence suggests the strategy is effective, it is not feasible to implement with the current research because the models do not consistently predict the regional effects.

Introduction

The impacts of climate change are becoming more destructive and the window of opportunity to reverse its effects is rapidly closing. Although there are many alternative energy solutions already available and under development, these alone are likely not enough to halt and/or reverse the effects of climate change. Geoengineering through solar radiation management is a proposed solution that may counter some of the damaging effects of increased CO₂ concentrations. Solar radiation management is the process of changing the stratospheric chemical composition to reflect greater amounts of solar radiation back into space. This has a cooling effect on the atmosphere which counteracts the warming effect of increased CO₂ atmospheric concentration. One of the most common geoengineering proposals involves using sulfate aerosols injected into the stratosphere to reflect greater amounts of solar radiation back out into space. Sulfate aerosols are the same aerosols created through chemicals released in volcanic eruptions.

The current body of research for sulfate aerosol injection involves initially studying the climate effect of volcanic eruptions into the stratosphere. Climate models are also used to study the proposed experiment with the GeoMIP suite of experiments being developed as a standard for easier comparison between models. The GeoMIP suite consists of experiments G1, G2, G3, G3S (optional), and G4. Each experiment has a reference climate (a climate without increased CO₂ and geoengineering), a climate pathway for increased CO₂, and a geoengineering climate. The reference scenario for G1 and G2 is PiControl (pre-industrial control) while G3, G3S, and G4 have reference scenario RCP4.5 between the years 2010 and 2029 (representative concentration pathway).

4.5 W/m^2). The climate changes scenarios are Abrupt 4xCO₂ which is an instantaneous quadrupling of pre-industrial CO₂ levels, 1pctCO₂ which is a 1% increase in CO₂ concentration per year, and RCP4.5 between the years 2030 and 2069 which is a more accurate estimate for future CO₂ concentration increases. The geoengineering scenarios G1, G2, and G3S merely balance a radiative forcing increase from CO₂ emissions with decreased radiative forcing for each CO₂ concentration scenario. Experiment G3 uses a feedback mechanism to inject aerosols at a rate that will return the temperature to pre-industrial levels while G4 injects aerosols at a constant yearly rate.

Physical experiments on the effects of volcanic eruptions are difficult due to ethical and practical concerns about releasing aerosol into the atmosphere and the distinction between research and the beginning of geoengineering. Additionally, the models developed (even if they use the same initial conditions) often reveal different results. The current disagreement in results from different models make it a somewhat impractical solution as the risks of its implementation are largely uncertain. This thesis compares the surface air temperature and precipitation changes between the paper *Impacts, effectiveness and regional inequalities of the GeoMIP G1 to G4 solar radiation management scenarios* (Yu et al., 2015) and the NCAR data outputs.

Chapter 1 covers the basic properties of aerosols. Chapter 2 explores the natural evidence that exists to support aerosols injection as an effective climate change mitigation strategy. This includes an exploration of the Little Ice Age as well as climate effects from modern volcanic eruptions. Chapter 3 focuses on the GeoMIP experiments and gives an overview of the model setup. Chapter 4 gives an overview of the procedure for data collection and comparison, while Chapter 5 gives the analysis of the results.

Part 1: Background Information

Chapter 1: Aerosols in the Atmosphere

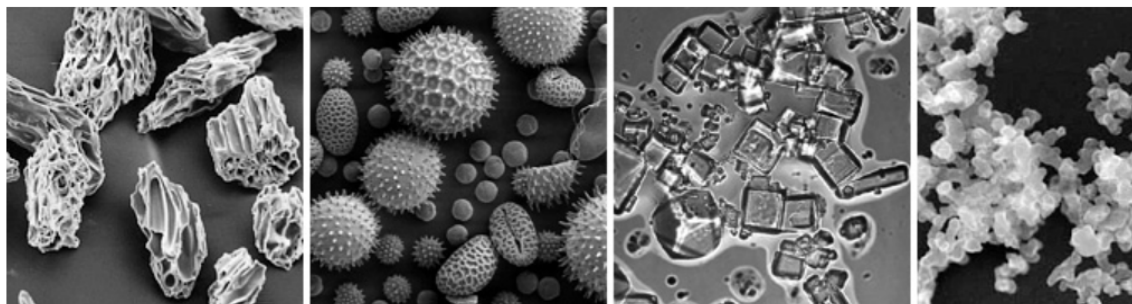
The term aerosol refers to the liquid and solid particles that exist within the atmosphere and can range in size from a couple nanometers to a couple thousand micrometers. They exist throughout the atmosphere from the lowest levels to the stratosphere. Aerosols are generally categorized by either their size and/or their chemical composition. Additionally, aerosols can be distinguished by having natural or anthropogenic (human-made) origins. Aerosol type and density is not uniformly distributed throughout the atmosphere and follows certain distribution patterns which are determined both by natural environmental trends as well as different types of human impacts. Typically, aerosols are only suspended in the atmosphere for short periods of time, but during that time they can travel very far distances. Few aerosols make their way into the stratosphere, but this allows them to remain for longer periods of time. Different aerosols will scatter or absorb light to varying degrees depending on their properties. An aerosol's ability to reflect or absorb incoming direct sunlight is called its "direct effect". The "indirect effect" refers to its influence in cloud formation and properties. Different properties of aerosols are measured using satellite's, aircraft, and ground-based instruments (Voiland, 2010).

Section 1: Categorization of aerosols

Aerosols are categorized based on their size and/or their chemical composition. In the field of toxicology, aerosols are identified as either ultrafine, fine, or coarse.

Meteorologists and regulatory agencies tend to call them particulate matter, PM_{2.5} or PM₁₀, depending on particle size. The size of the particle is relevant as smaller particles are more harmful to humans from a toxicology standpoint; they can penetrate further into the lungs. This can be seen in the image below, not only does aerosol size vary but their shapes are diverse (Voiland, 2010).

Figure 1: Electron microscope images (not to scale) highlight the diverse shapes of aerosols. The labels are volcanic ash, pollen, sea salt, and soot from left to right (Voiland, 2010).



Aerosols can also be categorized based on chemical composition, which includes the categories sulfates, organic carbon, black carbon, nitrates, mineral dust, and sea salt. These describe the primary types, but it should be noted that in the atmosphere different chemical types will form mixtures with other aerosols to form hybrids (Voiland, 2010). The aerosols produced from the output of volcanic eruptions are sulfates. This is the aerosol that is typically proposed for solar radiation management solutions and research. Additionally, there is research on solar radiation management using sea salt.

The origin of an aerosol is another useful way to differentiate between types. Most aerosols present in the atmosphere have a natural origin (~90%), while the minority consists of those with anthropogenic origins. Naturally occurring aerosols are vital to the composition and function of the atmosphere. Sulfuric aerosols are formed from the chemical output during volcanic eruptions. Other examples of naturally occurring

aerosols are the chemicals released from burning plant matter during forest fires. These primarily produce soot, black carbon, and brown carbon aerosols. The most abundant aerosols are sea salt and dust. They consist of minerals originating from desert sands and ocean spray. Aerosols with man-made origins come from the burning of fossil fuels along with biomatter. It can also come from sources such as by products of exhaust fuel. Usually, anthropogenic aerosols are smaller in size than their naturally occurring counterparts. From a toxicology standpoint, they tend to have a greater impact on health (Voiland, 2010).

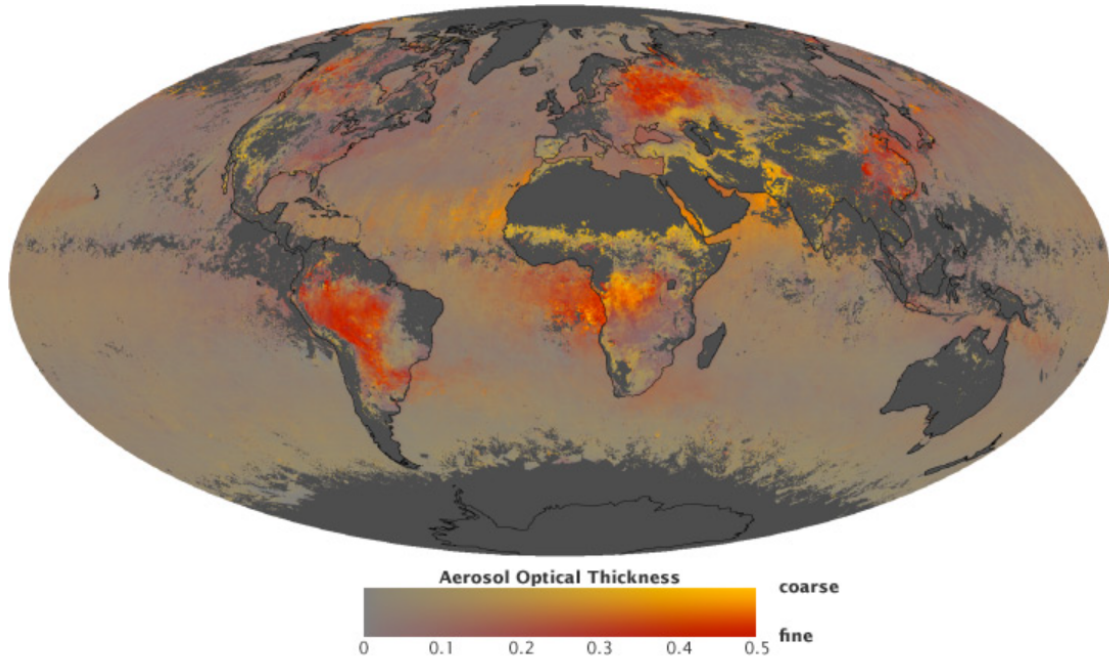
Figure 2: Natural aerosol sources such as desert dust, volatile organic compounds from vegetation, smoke from forest fires, and volcanic ash (Voiland, 2010).



Section 2: Aerosol Patterns

The type and density of aerosol is not evenly distributed throughout the atmosphere. Although aerosols can travel far from where they were initially released, atmospheric patterns cause an uneven distribution which can rapidly change across any given timeframe and location. Aerosol distribution throughout the atmosphere is also affected by anthropogenic factors like areas of high population which results in higher release of pollutants. These patterns can be observed in Figure 3 using satellite data (Voiland, 2010).

Figure 3: Map with global distribution of aerosols with proportions that are large or small (Voiland, 2010).



There are many examples of natural aerosol distributions. For example, a thinner layer of aerosols consisting of salt from whitecaps and sulfates from microalgae cover most of the oceans. Similarly, dust aerosols are formed above deserts. For anthropogenic origins, cities and other areas of high pollution can contribute to aerosol distribution. Eastern portions of the US and urban European areas have industrial aerosol plumes. These aerosols usually consist of sulfates from coal power and black organic carbon from vehicle traffic. This is observed above cities like New York, Pittsburgh, London, and Berlin. Anthropogenic aerosols are not only caused by industrial chemicals, but other human impacts to the environment like farming. Examples of these impacts are seen in California. The LA Basin becomes polluted with aerosols that include dust and wildfire smoke. Agriculture produces a large proportion of aerosols from newly processed earth that releases additional amounts of soil dust. The most aerosol heavy air is found in parts of Asia. These aerosols are so prevalent that satellites can detect a visible patch over

Bangladesh, Northern India, and Northern Pakistan. These aerosol clouds are caused by dust blowing from the Thar Desert and pollution from densely populated cities. Cities like Beijing in Eastern China can also produce dense aerosol layers from industrial pollution as seen in Figure 4 (Voiland, 2010).

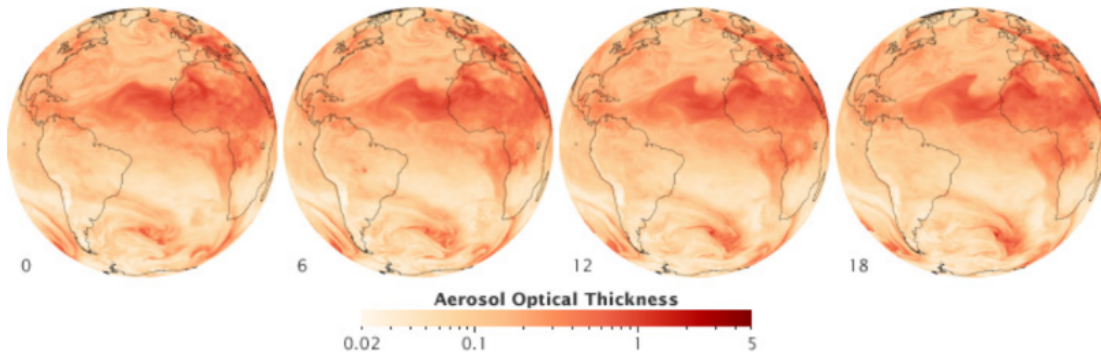
Figure 4: Beijing on October 9, 2010. The city is completely covered by air pollution (Voiland, 2010).



The Northern Hemisphere has mineral dust swirls over the deserts and other arid regions. Slash and burn agriculture in the Amazon and Central Africa releases large amounts of smoke and soot aerosols. Also fires that are set either by lightning or human activity during the summers in Canada, Russia, and the United States result in large aerosol production (Voiland, 2010).

Although aerosols are produced over certain areas, they are unlikely to remain where they were produced due the likelihood of being significantly displaced. Depending on factors like season and weather conditions they can potentially reach anywhere in the atmosphere. Most aerosols will only remain in the atmosphere for short periods, usually 4 – 7 days. In that time, they are still able to travel very far. For example, a particle that moves within the atmosphere at 5 m/s will be able to travel thousands of km in a week. This is how dust plumes from the Sahara Desert are frequently able to cross the Atlantic Ocean to reach the Caribbean as seen in Figure 5. Dust from the Gobi Desert and pollution from China are carried by winds to east Japan and the central Pacific Ocean. Even smoke from wildfires in Siberia and Canada can find their way to the Arctic Ice caps (Voiland, 2010).

Figure 5: On July 1, 2009, dust from North Africa travels over the Atlantic Ocean (Voiland, 2010).



Aerosol emission also changes over time. For example, man-made emission has increased due to growing urban populations and increasing industry in Asia while it has decreased in North America and Europe due to shifting industries and stricter pollution restriction policy. Natural events can also affect aerosol emissions. Historically, volcanic

eruptions and forest fires have emitted aerosols into the atmosphere that have changed global temperatures and weather patterns (Voiland, 2010).

Section 3: Direct and Indirect Effects

Aerosols and the clouds formed due to their atmospheric influence which reflect approximately 25% incoming solar energy back into space (Chin & Kahn, 2009). Different aerosols scatter and absorb sunlight to varying degrees depending on their properties. The scattering and absorbing potential of individual aerosols is referred to as the “direct effect” on Earth’s radiation field. The “indirect effect” refers to the impact that aerosols have in cloud formation that also works to cool the atmosphere. Aerosols present on the Earth’s surface also affect how reflective those different surfaces are, which has an impact on global temperatures (Voiland, 2010). Both effects are undeniably important in understanding how aerosols affect the environment as a whole and how they could be used to reduce and potentially reverse the effect of greenhouse gasses.

Most aerosols reflect sunlight back into space but not all. Whether an aerosol reflects or absorbs light is primarily dependent on the composition as well as the color of the particle. Bright colored as well as translucent aerosols tend to have higher reflectivity whereas darker aerosols absorb light. Pure sulfates and nitrates reflect almost all the radiation they encounter. This has the net effect of cooling the atmosphere. Black carbon alternatively absorbs radiation easily. This warms the atmosphere as seen in Figure 6. Organic carbon also called brown carbon or organic matter can also have a warming effect on the atmosphere, but it depends on the brightness of the ground below the atmosphere. Dust has varying degrees of influence on radiation because it depends on the

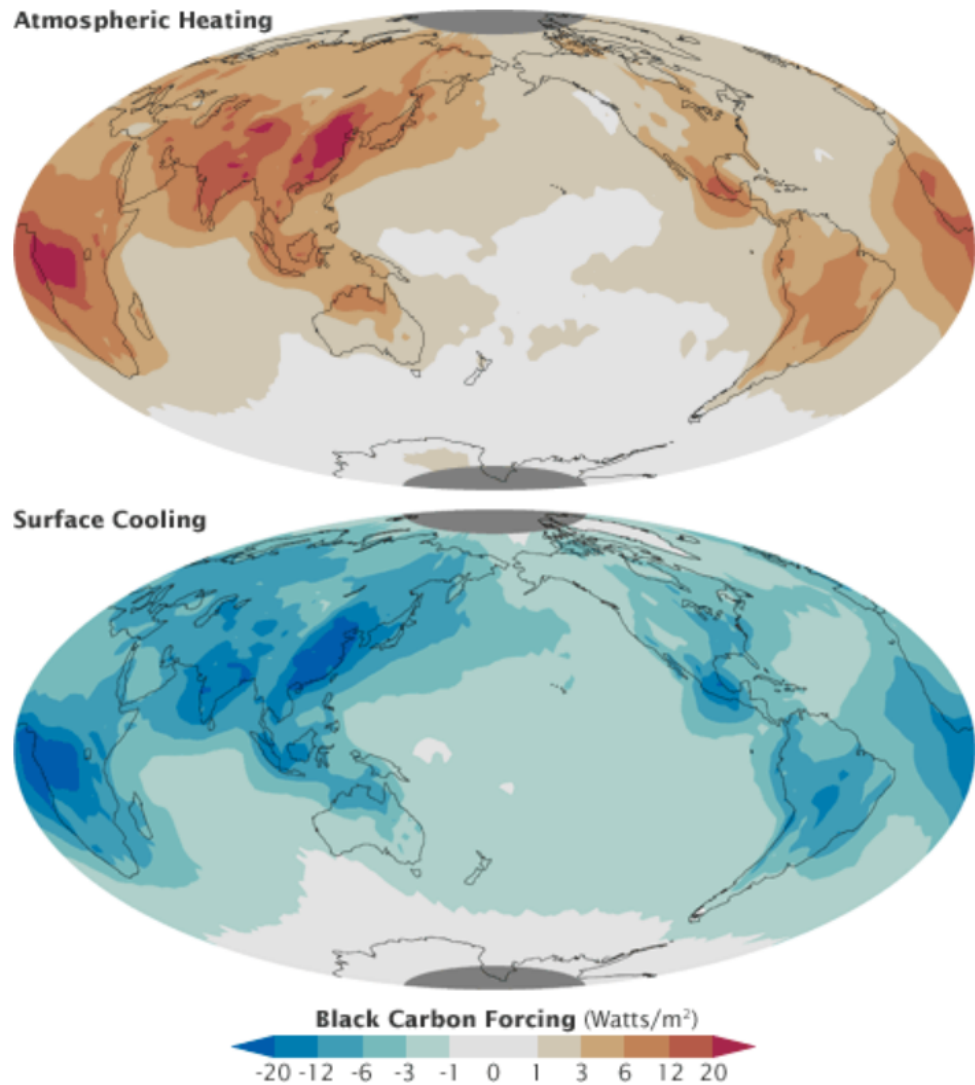
properties of the minerals that the dust is made up of. Salt particles usually reflect the entirety of the sunlight they meet (Voiland, 2010).

In addition to the effect that aerosols have on scattering and reflecting light in the atmosphere, they can also decrease planetary albedo. Bright surfaces on Earth, like white ice sheets, reflect radiation which will cool the climate. Alternatively, dark surfaces (like the ocean's surface) absorb radiation which will have a warming effect on the climate. Black carbon and other aerosols deposit a layer of dark residue on ice and other bright surfaces which will alter the reflectivity of that surface by making it lower. This has a warming effect, and the result that wildfires and industrial pollution have had on the arctic is evidence of this. The black carbon coming from these aerosol sources has dimmed the reflectivity of the ice caps which has hastened the warming process (Voiland, 2010).

Although the individual direct effects of aerosols are somewhat understood, their net effects in the atmosphere are still largely uncertain and creating accurate models is an ongoing area of research. There are few climate models that take the effect of non sulfate aerosols into consideration as the specifics of modeling these effects is an area of new research. All effects described in this section are estimation based on climate measurements and modeling which have limited accuracy (Voiland, 2010). In order to improve climate models, the effects of aerosols, which are often the source of the highest uncertainties, must be better understood. The difficulties of modeling aerosols comes from the high spatial and temporal variation of the amount and properties of aerosols. The interaction of aerosols with clouds and precipitation add another layer of complexity.

Better observation of aerosols in the atmosphere as well as better modeling is needed for more accurate aerosols effects estimates (Chin & Kahn, 2009).

Figure 6: Black carbon absorbs sunlight instead of reflecting it. This warms the layer of the atmosphere carrying the black carbon. Due to the color of the aerosol, it also shades and cools the surface below. This shading is counteracted by heat radiating from the warmer atmosphere. These conflicting effects highlight the complexity and uncertainty associated with studying aerosols in the atmosphere (Voiland, 2010).

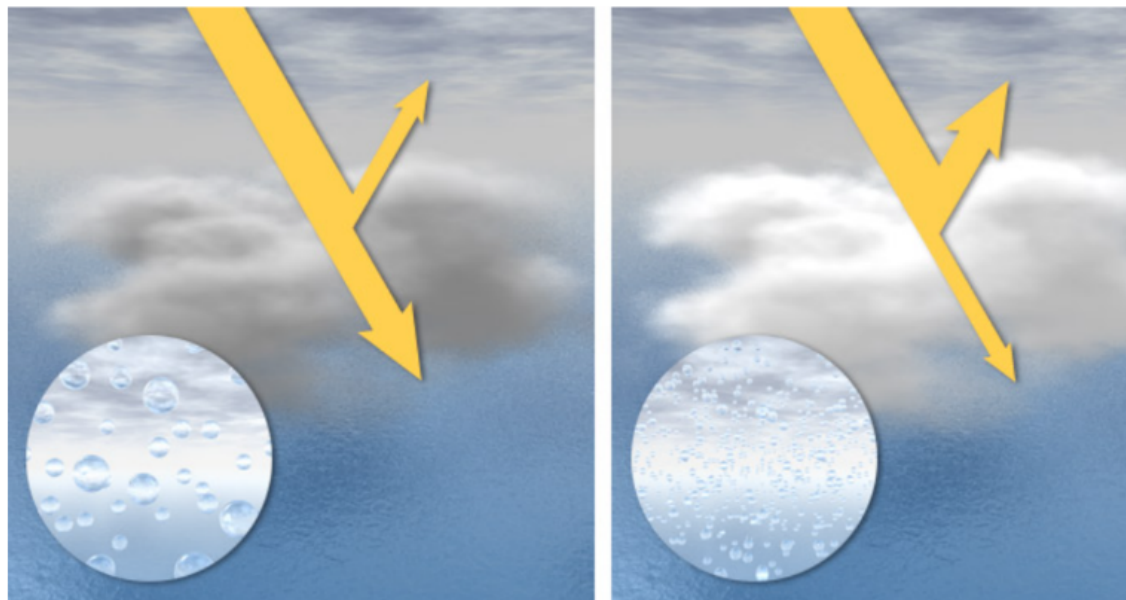


Overall, scientists believe that sulfates and similarly reflective aerosols outweigh the effects of the absorptive aerosols like black carbon. Some models have predicted that

aerosols, naturally occurring and anthropogenic, have cut the overall global warming effect by 50% (Chin & Kahn, 2009). However, one aspect of aerosols to remember is that they do not tend to distribute themselves randomly throughout the atmosphere and have more local effect than other greenhouse gasses (Voiland, 2010). This means that stratospheric aerosol injection solutions may combat rising temperatures globally, but the local effects will be varied and hard to predict.

The “indirect effect” that aerosols have on the atmosphere is related to cloud formation. This has a counteractive effect on global warming on the global scale. Part of the reason that aerosols have a more diverse local effect and do not disperse the same way that greenhouse gasses do is because of their effect on cloud formation. Aerosols serve as cloud condensation nuclei and are vital to the formation of clouds. Naturally occurring aerosols like sulfates, sea salt, or ammonium salts are most common condensation nuclei in environments with low pollution. Alternatively polluted air has a higher density of water-soluble particles. This results in polluted clouds having smaller but greater numbers of droplets. These small droplets result in brighter clouds. This is because they scatter the light more and therefore polluted clouds tend to be more reflective than those made from naturally occurring aerosols as is seen in Figure 7. This produces a greater net cooling effect as it blocks sunlight that would normally reach the Earth. This effect is referred to as the “cloud albedo effect” (Voiland, 2010).

Figure 7: Clouds in clean air consist of a small number of large droplets (left). These are darker and translucent. In air with high concentrations of aerosols, water easily condenses into particles resulting in clouds consisting of many small particles. These clouds are dense and bright (Voiland, 2010).



Although the overall effects that aerosols have on the atmosphere are not widely understood, it is generally believed that aerosol seeded clouds cool Earth's surface through the shading which covers about 60 percent of the surface. They also do this through increasing the reflectivity of the atmosphere. This is promising for a solution that would seek to reverse the effects of greenhouse gasses as the clouds have a very significant impact on temperatures. However, while aerosols and clouds affect temperatures locally, greenhouse gasses have a global impact. This makes characterizing the potential effects very difficult (Voiland, 2010).

In addition to affecting the reflectivity of clouds, aerosols also influence precipitation. In general, it is thought that they suppress precipitation, but this is not universally true. Aerosols that decrease the size of droplets will also decrease

precipitation opportunities as larger droplets are more likely to precipitate. Black carbon has been observed to decrease precipitation. Studies done on pollution over the Indian Ocean as well as biomass smoke from fires in the Amazon show that black carbon warms the atmosphere which evaporates cloud droplets and decreases precipitation. The clouds will become hazy, an effect referred to as the “semi direct effect.” (Voiland, 2010).

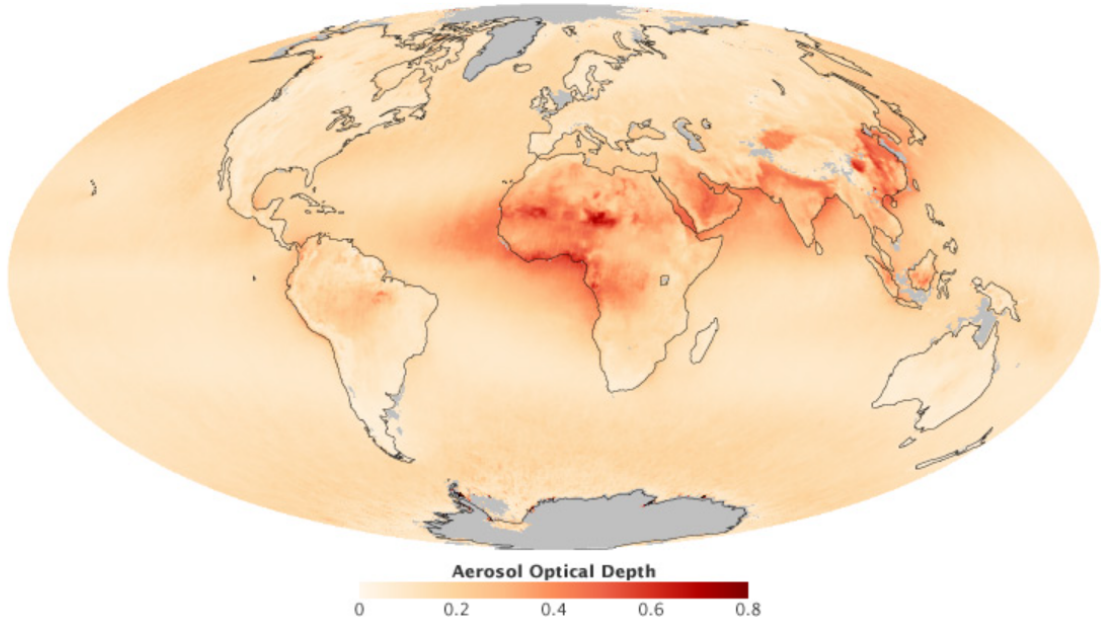
Averaged over the globe, current estimates indicate that aerosol indirect effect counteracts less than half of the warming of greenhouse gasses (Chin & Kahn, 2009). Indirect effects are not well understood and are unpredictable and vary greatly in space and time. There is also not a good way to measure aerosol content of clouds. Clouds are one of the greatest uncertainties in climate prediction (Voiland, 2010). The difficulty in understanding indirect effects of aerosols limits the accuracy of model estimates of aerosol injection strategies.

Section 4: Measurement of Aerosols

Currently satellites, aircraft, and ground-based instruments can be used to test aerosol content in the atmosphere. The most important and commonly used tool available are radiometers, an instrument that records the amount of electromagnetic radiation. The reported value is the aerosol optical depth (AOD) which is a measure of the quantity of light that aerosols scatter or absorb in the atmosphere. Optical depth of less than 0.05 is indicative of clear skies with few aerosols and maximum visibility. Alternatively optical depth above 2 or 3 indicate high concentrations of aerosols. Another measurement used is single scattering albedo (SSA), which is the fraction of light scattered compared to the total. These values range from 0.7 for highly absorbing particles to 1 for aerosols that can

only scatter light (Voiland, 2010). The table at the end of this section gives some of the measurements for common aerosol types.

Figure 8: Average distribution of aerosols from June 2000 through May 2010 as measured by the Multi-angle Imaging Spectroradiometer (MISR) (Voiland, 2010).



The first satellite that was able to monitor aerosol optical depth from space was the Advanced Very High Resolution Radiometer (AVHRR) in the 1970s. This got optical depth from measurements made in the visible and near infrared spectrum and was a passive radiometer that measured intensity of sunlight reflected off aerosols using the dark ocean as the background. Since the 1970's instrumentation has become more accurate and sophisticated, which has made it possible to study aerosols over land mass instead of just the oceans. The Multi-angle Imaging Spectroradiometer (MISR) and the Moderate Resolution Imaging Spectroradiometer (MODIS) can view aerosols at different angles and wavelengths, which gives more accurate results (Voiland, 2010).

The Cloud Aerosol Lidar and Infrared Pathfinder Satellite Observer (CALIPSO) utilizes laser technology, which gives vertical profiles of the aerosol plumes and clouds. The Polarization and Directionality of the Earth's Reflectances (POLDER) gives information on the polarization of the light as it goes through the atmosphere. This was not measured until this instrument was utilized and it is helpful in figuring out the particle type being measured. The Aerosol Polarimetry Sensor (APS) is even more tuned to polarized light (Voiland, 2010).

Ground-based sensors are used in addition to satellite data to validate and sometimes give more accurate measurements. For example, NASA co-sponsored a global network of on ground sensors called Aerosols Robotic Network or AERONET. It consists of over 200 sun photometers which can measure the aerosol optical depth around the world. They work by measuring the intensity of light under cloud free conditions. Although progress has been made in measuring aerosols, it is still very challenging to characterize the competing impact of aerosols against greenhouse gasses and different types of aerosols. Additionally, measuring aerosols in clouds is challenging due to the hybrid aerosols that form when different aerosol types clump together. Also, humidity and temperature fluxuations can change the way the aerosols behave within the clouds (Voiland, 2010).

Table 1 gives the estimated source strengths, lifetimes, and amount for the common aerosol types. These values are based on the aggregate emission estimates in addition to global model simulations. The total source refers to the amount released per year into the atmosphere. The lifetime is the time that the aerosol spends in the atmosphere. The mass loading refers to the amount of aerosol in the atmosphere at a

particular time. The aerosol optical depth (AOD) or aerosol optical thickness (AOT) is the amount of incident light that is either scattered or absorbed by airborne particles (Chin & Kahn, 2009).

Table 1: Properties of common chemical aerosol types including total source, lifetime, mass loading, and optical depth (Chin & Kahn, 2009).

Category	Total Source (Tg/yr)	Lifetime (day)	Mass loading (Tg)	Optical Depth @ 550nm
	Median (Range)	Median (Range)	Median (Range)	Median (Range)
Sulfates	190 (100-230)	4.1 (2.6 - 5.4)	2.0 (0.9-2.7)	0.034 (0.015-0.051)
Particulate organic matter	11 (8-20)	6.5 (5.3 -15)	0.2 (0.05-0.5)	0.004 (0.002-0.009)
Black carbon	100 (50-140)	6.2 (4.3 - 11)	1.8 (0.5-2.6)	0.032 (0.012-0.054)
Dust	1600 (700-4000)	4.0 (1.3 - 7)	20 (5-30)	0.030 (0.020-0.067)
Sea salt	6000 (2000 - 120000)	0.4 (0.03 -1.1)	6 (3-13)	0.13 (0.065-0.15)

Chapter 2: Natural Evidence for Aerosol Atmospheric Cooling

Even without the use of complex climate models, the cooling effects of aerosols on the climate have been observed through climate data collection after an eruption event that released significant amounts of aerosols into the atmosphere. Since aerosols released into the lower atmosphere below and at cloud cover generally do not stay in the atmosphere for longer than a week, they do not have significant long-term impacts on climate. Aerosols that make their way into the stratosphere can stay there for years as they are above the area in the atmosphere where clouds form and are less likely to be released back to earth through precipitation. An aerosol injection strategy would aim to deposit aerosols into the stratosphere to increase longevity of aerosol impact. Strong volcanic eruptions can release aerosols with enough force that they will make their way into the stratosphere where they can remain for several years. Data collected from such eruptions indicates that such aerosols have a cooling effect on climate which is promising for the development of an aerosol injection climate solution.

Section 1: The Little Ice Age

The Little Ice Age is the longest, most recent period of mountain glacier expansion and occurred in the 16th to the middle of the 19th century (Bradley & Jonest, 1993). During this period, the European climate was most impacted. The beginning of the period is marked by a trend towards enhanced glacial conditions in Europe. These conditions followed the warmer conditions of the medieval warm period (medieval climatic optimum of Europe). The period ends with a dramatic retreat in glacier size during the 20th century. Although other areas experienced periods of cooling (expanding

glaciation, and altered climate conditions during this time) this was highly variable from region to region and throughout time. The Little Ice Age is therefore not in reference to a global ice age, but rather a local phenomenon to Europe. Quantitatively, the Little Ice Age is characterized by cooling of about 0.6 degree Celsius in the Northern Hemisphere during the 15th through 19th centuries (Mann, 2002).

Various sources of evidence point to the Little Ice Age occurring in Europe and other regions neighboring the North Atlantic during the 16th and 19th centuries. The evidence includes documentary accounts of mountain glacial retreats and advances, historical documentation of weather conditions, and some centuries long thermometer measurements. Documentary accounts include artist renditions of the same area during different time periods. Figure 9 is paintings of the French and Swiss Alps made before and after the glaciers advanced and retreated. There is a substantial difference in glacier size (Mann, 2002).

Figure 9: Portrait of Argentiere glacier in the French Alps from an etching made between 1850 and 1860 (left) and a modern photograph of the glacier taken in 1966 (Mann, 2002).



Historical records of the impacts of these glacial, temperature, and weather changes is another source of documentary evidence. In the Chamonix valley, near Mont Blanc, France, farms and villages were destroyed due to the advance of mountain glacier fronts. This was so devastating that the Bishop of Geneva was called and performed an exorcism of dark forces. Additionally, the colder conditions and changing weather has been linked to crop failure in Northern European areas during the time. These reports include mention of famine, disease, and higher child mortality rates which are hypothesized to be related to the decreasing temperatures and changing weather conditions (Mann, 2002).

It is unclear whether the greatest impacts of the time were due to the decreasing overall temperature or due to an increase in the variability of the weather conditions. The most extreme changes were not happening on an annual time frame but rather were contained to specific seasonal changes. For instance, particularly cold winters began in Switzerland in the 1550s while cold springs began in 1568 and the year 1573 has its first cold summer. The increased variability in some cases leads to colder winters and relatively warm summers. For example, the cold winter and then warm summer that occurred in 1666 caused the Great Fire of London. Similarly, another cold winter followed by warm summer could have added to peasant discontent and the storming of the Bastille in Paris during summertime of 1789 (Mann, 2002).

Outside of Europe and the North Atlantic region, a large-scale Little Ice Age is less clear. The evidence does not support a continuous global cooling period outside of the European and the North Atlantic region. The evidence does however suggest a trend towards cooler temperature from the 13th through 19th centuries which is variable region

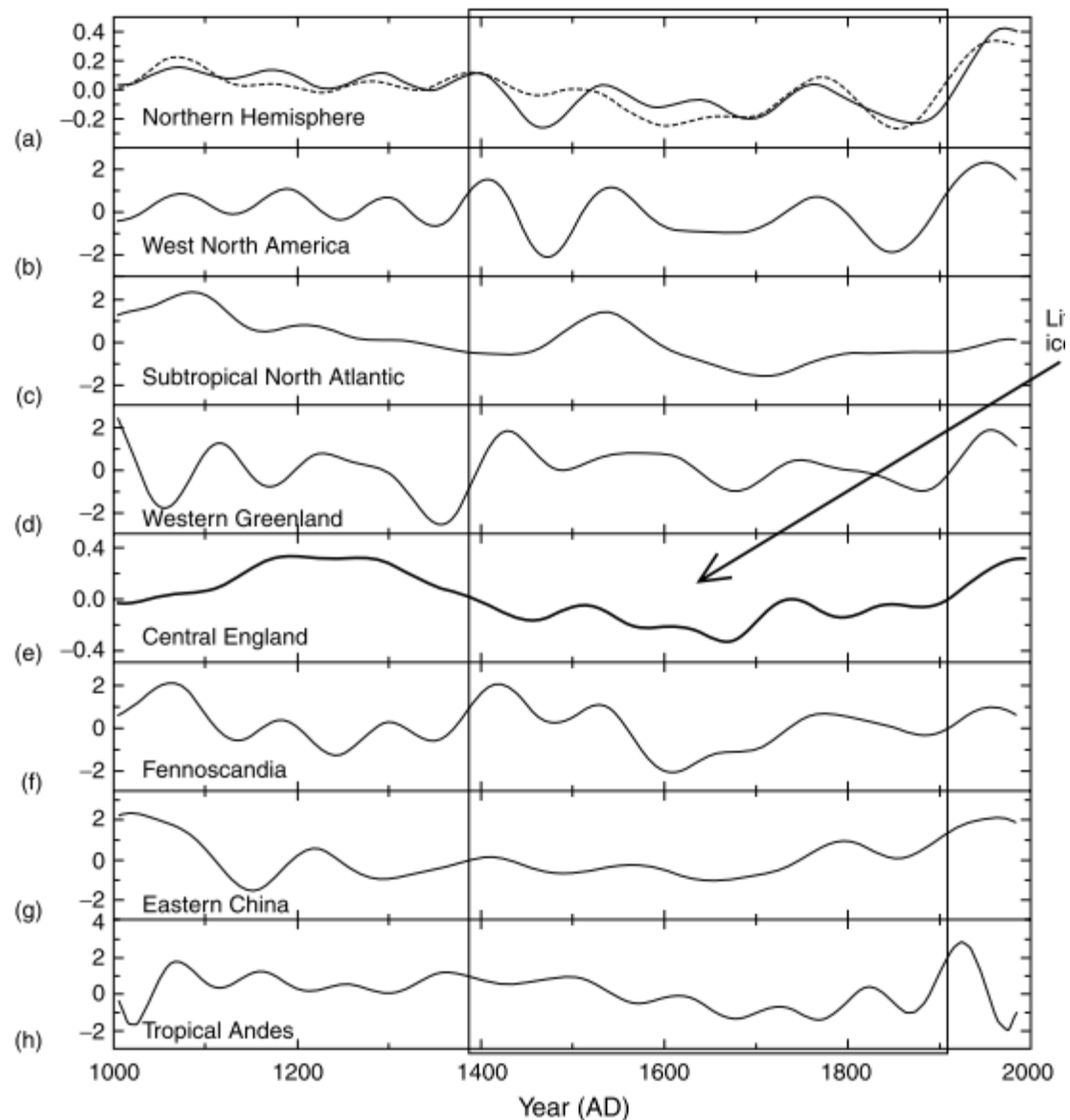
to region and is broken by periods of warming (Bradley & Jonest, 1993). Measurement is challenging outside of Europe and the North Atlantic as direct indications of climate variation like long time thermometer measurements and historical documentation is not as prevalent. The evidence that does exist is long instrumental climate records in North America during the middle of the 18th century and documentary evidence from Canada and the northeastern US. This evidence came from European settlers and Native Americans in western North America. This evidence provides a mixed picture of the climate during this time. An example of the discrepancy is in the 17th century, which was the coldest for Europe, there does not appear to be any indication of climate changes in North America while in the 19th century, a warmer time in Europe, there are records of decreasing temperatures. For instance, New York Harbor was reported to have frozen during periods in the 19th century. Additionally, there is human documented evidence in China and Russia that also give different patterns of climate change than Europe and North America (Mann, 2002).

Although historical documentation and temperature measurements from other regions are limited, there are indirect geological measurements that can be made to estimate temperatures and climate changes in different regions during this period. The positions of moraines or tills that are left behind due to the receding of glaciers are used to characterize when glaciers advanced and receded in these regions. This evidence suggests that there was an increase in glacial mass in Alaska, New Zealand, and Patagonia before the 20th century. The timing of these changes was not synchronized which indicates that this was not a coordinated event that would be a result of a global increase in glaciers. Glacier activity alone is not a good metric for determining climate

and temperature changes due to the many factors that can explain glacier activity. An example of this is that increased glacial mass can be caused by increased winter precipitation as well as lower summer temperatures. Also, glaciers due to their size respond relatively slowly to climate changes. The effects of a climate could be delayed by decades or centuries (Mann, 2002).

Due to glacial information being unable to paint the full climate picture, additional information is needed to assess climate changes in these regions during these time periods. Historical records can be supplemented with proxy climate records like growth and density from tree rings, laminated sediment cores, annually resolved ice cores, isotropic indicators from corals, and long-term ground temperature trends from borehole data. These indirect measures are somewhat unreliable due to the influence that non-climate related effects have on them, the seasonal nature of the records, and the lack of independent data to compare with. However, these records have been used to estimate temperature and climate changes in different regions. Figure 10 shows these changes (Mann, 2002).

Figure 10: Estimated relative temperature variations in °C during the past millennium for different regions. The records are smoothed to highlight century and other long-term variations. Part (a) refers to the Northern Hemisphere mean temperatures with the solid line being the annual mean temperature over the entire hemisphere and the dashed line over the extratropical regions only during the warm season; these values are based on global databases on proxy climate indicators like the tree rings and ice core data. Part (b) is the tree ring data from western North America and part (c) is sediment records from the Sargasso Sea of the North Atlantic. Part (d) is ice cores from western Greenland while part (e) is thermometer, historical, and proxy data from central England. This indicates the European Little Ice Age which is labeled. Part (f) contains tree ring data from Fennoscandia and phenological evidence originating from Eastern China. Part (h) is ice core data from the tropical Andes in South America (Mann, 2002).



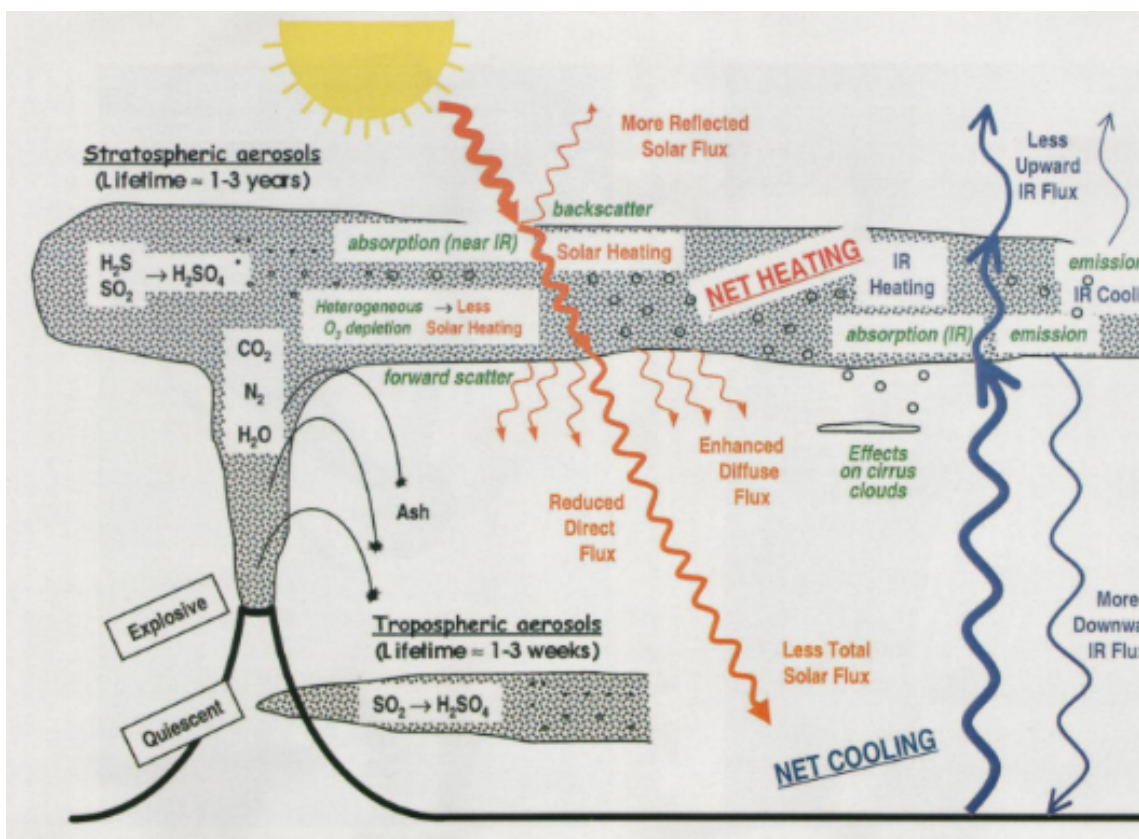
Although the evidence strongly points towards the occurrence of the Little Ice Age, the factors that cause this period are under debate. The period occurred before human influence on global climate. Some of the long-term cooling observed is attributed to astronomical factors like the dimming of solar radiation. These factors are not able to explain the short and extreme cooling that was observed in many regions during this time. One explanation is that the sunlight was reflected by sulfate aerosols from volcanic explosions that were prevalent in the early to the mid 19th century. An example of an eruption occurring during this period is the 1815 eruption of Tambora in Indonesia that is generally cited as the cause of the year without a summer. The pattern of weather changes with cooling in eastern North American and Europe and warming in western US and the Middle East is consistent with the relationships between volcanic forcing and the North Atlantic Oscillation. This observation and theory support the volcanic explanation. Additionally, the sun increased its output in the 18th century by 0.25 percent after what is referred to as the Maunder Minimum of the 17th century. This is another explanation for the cooling period. Additionally, changes in ocean circulation could have increased the temperature changes being experienced (Mann, 2002).

Section 2: Major Radiative Processes of Major Volcanic Eruptions

Volcanic aerosols have an effect on radiative forcing in the atmosphere. Figure 11 outlines the major radiative processes that result from a stratospheric aerosol cloud formed due to a major volcanic eruption. The eruption produces plumes of SO₂, CO₂, and H₂. The CO₂, H₂, and H₂O fall back to Earth as ash while SO₂ and H₂S combine to form sulfate aerosol H₂SO₄. Some of the aerosols reach the troposphere where they remain for

1-3 weeks while the aerosols that make it into the stratosphere remain for 1-3 years. The aerosols in the stratosphere have atmospheric and climatic effects.

Figure 11: Volcanic atmospheric inputs and their effects. The text in black is the atmospheric inputs and their descriptions. The text in green refers to the phenomena caused by the aerosols: backscattering, scattering, absorption (near IR), emission, O₂ depletion, and “indirect effects”. The effects in red correspond to changes in solar flux while blue corresponds to changes in IR flux. The net effect is less solar flux at the surface and IR heating of the atmosphere (Robock, 2000).



The most noticeable impact is the effect on solar radiation. The sulfate particles are about the same size as visible light, effective radius of $0.5 \mu\text{m}$, and they have a single scatter albedo of 1 meaning that they scatter solar radiation. Figure 11 highlights that the light is either backscattered or forward scattered. The light that is backscattered to space increases the net planetary albedo and reduces the amount of solar energy that reaches the

Earth's surface. Backscattering is dominant at the surface and results in a net cooling there. Alternative to backscattering, solar radiation is also forward scattered. This results in enhanced diffuse flux which compensates for some portion of the reduced direct flux from sunlight. The O₂ layer is also depleted by sulfate aerosols which decreases solar heating as shown in Figure 11 (Robock, 2000).

The IR spectrum of light actually results in net heating in the atmosphere. IR radiation is absorbed or emitted. More IR radiation is absorbed than is emitted which results in more downward IR radiation flux and less upward radiation flux. The net IR effect is heating in the atmosphere. The net effect of all spectrums of light at the surface is cooling. This is observed after volcanic eruptions (Robock, 2000).

To examine volcanic eruption effects on climate, radiative forcing calculations due to aerosols are necessary. For radiative disturbances that are evenly spread globally such as changes in greenhouse gas concentrations, radiative forcing is the change in the net radiative flux at the tropopause. The net radiative flux refers to the balance between increased and decreased radiative forcing due to different factors. For aerosols with varied vertical and horizontal distribution, the complete calculation of radiative forcing includes changes in net fluxes at the tropopause as well as the vertical distribution of atmospheric heating rates, the change of downward thermal, and net solar radiative fluxes at the surface (Robock, 2000). Calculating radiative forcing changes from CO₂ concentration is much simpler than calculating the radiative forcing changes due to sulfate aerosols as all the different competing effects from Figure 11 must be accessed to determine the net effect.

Section 3: Major Volcanic Eruptions into the Stratosphere

The effects of volcanic eruptions during the Little Ice Age are difficult to measure accurately due to the difficulties discussed in Section 1. However, there have been large eruptions that have had measurable effects on climate more recently. Data collected from more recent eruptions indicates that volcanic aerosols have a cooling effect on the climate. These observations give insight into the cooling effects of aerosols and provide a foundation for aerosol injection as a proposed climate solution.

The volcanic eruptions mentioned in this section are large enough so that the sulfate aerosol released travel above the cloud layer and into the stratosphere. These volcanic eruptions are more important to study because they give greater insight into the effects of aerosols in the stratosphere and are longer lasting than those without enough force to inject sulfate particles into the stratosphere.

Table 2 summarizes the units used to characterize aerosol loadings of volcanic eruptions. These units were defined based on surveys of volcanic eruptions performed using various historical data sources that indicate observations of the eruptions. Table 3 gives the names of the volcanoes that had a major eruption in the last 250 years. The value given for Askja, Iceland is the Southern Hemisphere signal only and probably not related to Askja (Robock, 2000).

Table 2: Volcanic units description (Robock, 2000).

Name	Units	How calculated
Dust veil index (DVI)	Krakatau = 1000	Sunsets, eruption, and radiation observations
Mitchell	Aerosol mass	Based on the DVI
Volcanic explosivity index (VEI)	Krakatau = 6	Explosivity, from geological and historical reports
Sato	$\tau (\lambda = 0.55 \mu m)$	Radiation and satellite observations
Ice core volcanic index (IVI)	$\tau (\lambda = 0.55 \mu m)$	Average of ice core activity or sulfate measurements

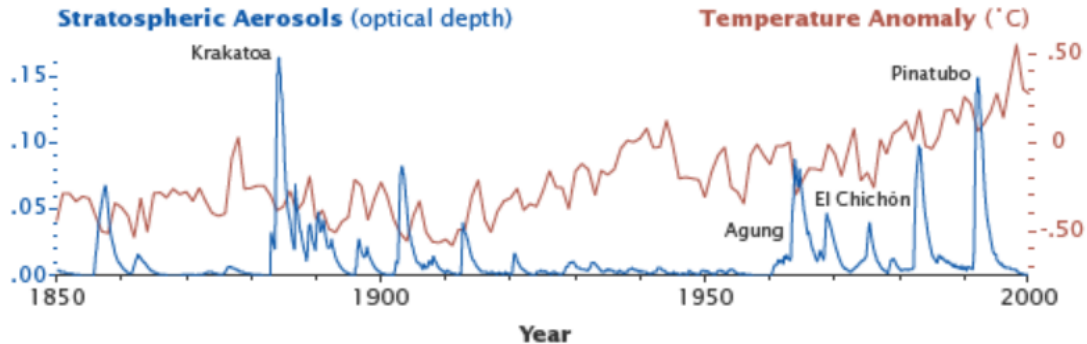
Table 3: Major volcanic eruptions in the last 250 years (Robock, 2000).

Volcano	Year of Eruption	VEI	DVI/E _{max}	IVI
Grimsvotn [Lakagigar], Iceland	1783	4	2300	0.19
Tambora, Sumbawa, Indonesia	1815	7	3000	0.50
Cosiguina, Nicaragua	1835	5	4000	0.11
Askja, Iceland	1875	5	1000	0.01
Krakatau, Indonesia	1883	6	1000	0.12
Okataina [Tarawera], North Island, New Zealand	1886	5	800	0.04
Santa Maria, Guatemala	1902	6	600	0.05
Ksudach, Kamchatka, Russia	1907	5	500	0.02
Novarupta [Katmai], Alaska, United States	1912	6	500	0.15
Agung, Bali, Indonesia	1963	4	800	0.06
Mount St. Helens, Washington, United States	1980	5	500	0.00
El Chichon, Chiapas, Mexico	1982	5	800	0.06
Mount Pinatubo, Luzon, Philippines	1991	6	1000	...

All eruptions listed have had noticeable atmospheric and climatic effects. The 1783 eruption in Iceland had an impact on the European summer. The 1815 Tambora eruption produced the 1816 year without summer. The effects of the Krakatau eruption were studied by the Royal Society in London. The studies include extensive watercolors detailing volcanic sunsets near London. The book includes microbarographs of pressure waves for four circuits of the globe that were measured with microbarographs. This makes this explosion likely the loudest in recent times. The 1963 eruption produced the largest stratospheric dust veil in 50 years and as a result it has been studied extensively. The Mount St. Helens eruption was very explosive but did not inject large amounts of sulfur into the stratosphere and therefore did not have large global effects (Robock, 2000).

The most recent large explosion, Mount Pinatubo in the Philippines occurred in 1991. This eruption ejected over 20 million tons of sulfur dioxide as high as 60 km above Earth's surface. The aerosols ejected that high into the stratosphere remained in the atmosphere and only settled out after several years. It was theorized at the time sulfate aerosols had a cooling effect so climatologists predicted a fall in global temperature due to the sulfate injection into the stratosphere. As can be seen in Figure 12, the global temperature dropped by 0.6°C for 2 years (Voiland, 2010).

Figure 12: The temperature anomalies and optical depth for Krakatoa, Agung, El Chichón, and Pinatubo over time (Voiland, 2010).



Volcanic eruptions can inject tens of Tg of active gasses and solid aerosol particles into the atmosphere. This affects the Earth's radiative balance and climate by disturbing the stratospheric chemical balance. After an eruption, the volcanic cloud forms over several weeks by SO_2 conversion to sulfate aerosol. The result is a cloud of sulfate aerosol particles that has an impact on the shortwave and longwave radiation. This disturbance to the atmospheric equilibrium affects surface temperature due to both direct radiation effects and indirect effects on atmospheric circulation and cloud formation. In cold regions of the stratosphere, the aerosol particle also functions as a location for chemical reactions that free chlorine which destroys ozone (Robock, 2000).

Section 4: Weather and Climate Response

The long-term climate effects of volcanic eruptions are still debated although there is evidence to suggest that they can have influence on climate even on 100-year timescales. The individual, shorter term effects are well documented and understood. Large single eruptions can produce global or hemispheric cooling for 2 to 3 years (Bradley & Jonest, 1993). The winters after large tropic eruptions are warmer in the

Northern Hemisphere. Additionally, volcanic aerosols provide an area for chemical reactions that destroy ozone. Ozone depletion was observed following Pinatubo. Table 4 summarizes these climate effects (Robock, 2000).

Table 4: Weather and climate effects of large explosive volcanic eruptions (Robock, 2000).

Effect	Mechanism	Begins	Duration
Reduction of diurnal cycle	Blockage of shortwave and emission of longwave radiation	Immediately	1 – 4 days
Reduced tropical precipitation	Blockage of shortwave radiation, reduced evaporation	1 – 3 months	3 – 6 months
Summer cooling of NH tropics and subtropics	Blockage of shortwave radiation	1 – 3 months	1 – 2 years
Stratospheric warming	Stratospheric absorption of shortwave and longwave radiation, dynamics	1 – 3 months	1 – 2 years
Winter warming of NH continents	Stratospheric absorption of shortwave and longwave radiation, dynamics	½ year	One or two winters
Global cooling	Blockage of shortwave radiation	Immediately	1 – 3 years
Global cooling from multiple eruptions	Blockage of shortwave radiation	Immediately	10 – 100 years
Ozone depletion, enhanced UV	Dilution, heterogeneous chemistry on aerosols	1 day	1 – 2 years

After Mount St. Helens erupted, scientists observed a reduction of the diurnal cycle. The eruption caused a large lateral volcanic plume to be deposited into the troposphere locally. As far as 135 *km* east of the eruption, it was dark enough that street

lights turned on during the middle of the day. The aerosol layer from the explosion separated Earth's surface from the top of the atmosphere. The surface air temperature cooled by as much at 8°C during the day and warmed by as much as 8°C at night. This reduction in the diurnal cycle only occurred for a few days, it ceased once the aerosol cloud dispersed. After the Krakatau eruption, scientists observed a similar effect. It should be noted that the St. Helens eruption had a large local effect as described above but since its stratospheric sulfur input was small it had minimal global climate impact (Robock, 2000).

Summer cooling is observed after volcanic eruptions and is due to direct radiative forcing of the surface accompanied by a reduction in total downward radiation which has a net cooling effect on the surface. In the tropics and midlatitude regions during the summer, these effects are larger than other climatic effects as there is more sunlight that can be blocked. Model simulations have revealed that maximum cooling happens approximately 1 year after an eruption and it is of 0.1 – 0.2 °C magnitude. This cooling is displaced towards the Northern Hemisphere. This is because land surfaces respond more quickly to radiation perturbation and therefore the Northern Hemisphere has greater sensitivity to radiation reduction due to volcanic aerosols. Model simulations have also found reduced tropical precipitation in the 1 to 2 years following these large eruptions. This is due to cooling after eruptions which limits evaporation that fuels the local global hydrological cycle (Robock, 2000).

Stratospheric heating following injection from volcanic aerosols is well supported. This heating is caused by the absorption of both near-IR solar radiation at the top layer and terrestrial radiation at the bottom. In stratospheric temperature trends, as

observed in Figure 13, there are two strong signals that correspond to the El Chichon eruption and the Pinatubo eruption. The temperature rose about 1 °C in both cases but this lasted for 2 years for Chichon and about 4 years for Pinatubo. It should be noted that this goes against the trend of stratospheric cooling that occurs due to ozone depletion and increased CO₂ which are caused by anthropogenic impacts (Robock, 2000).

Figure 13: Global average monthly stratospheric temperatures from satellite observation. The times of El Chichon and Pinatubo eruptions are labeled with arrows (Robock, 2000).

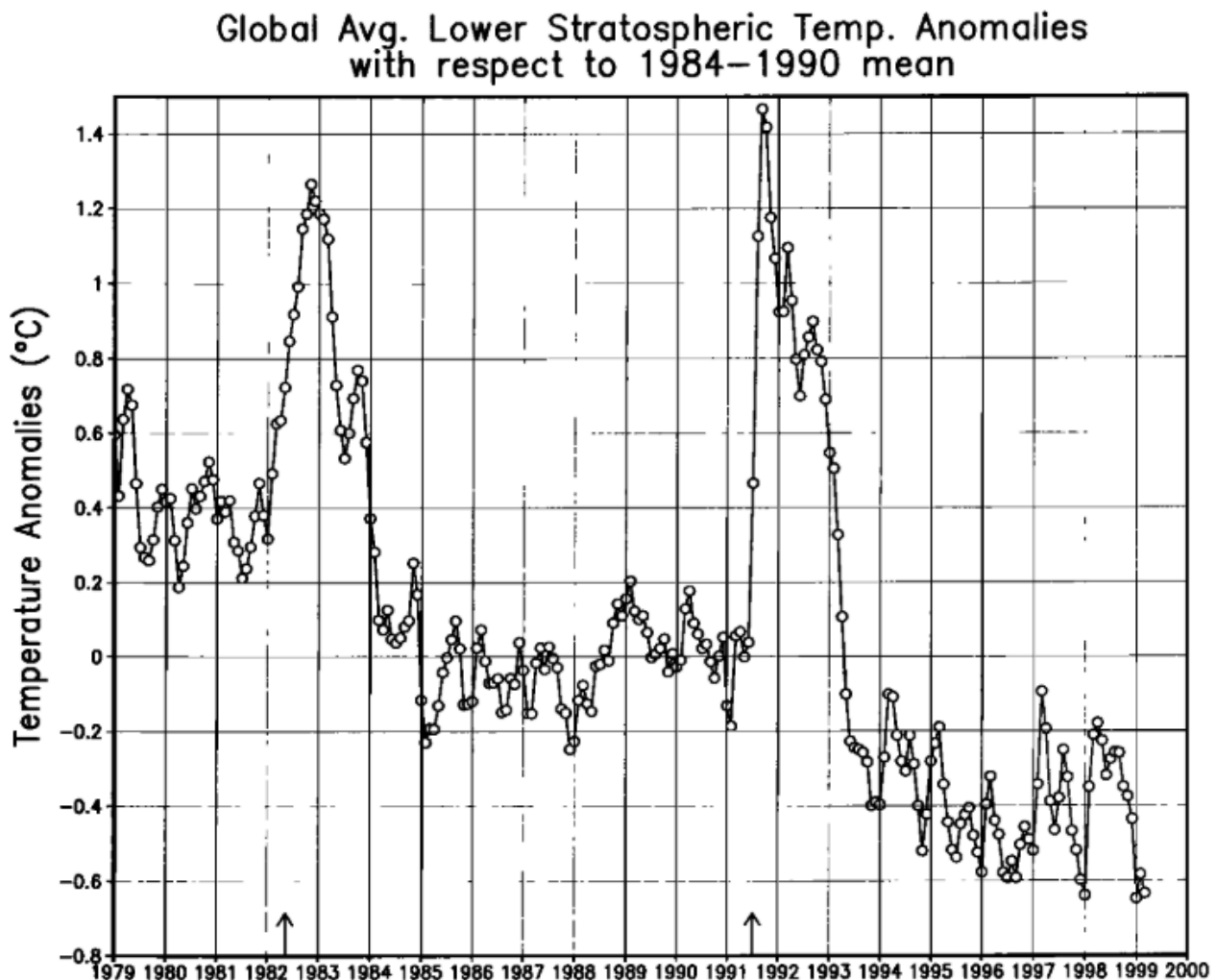
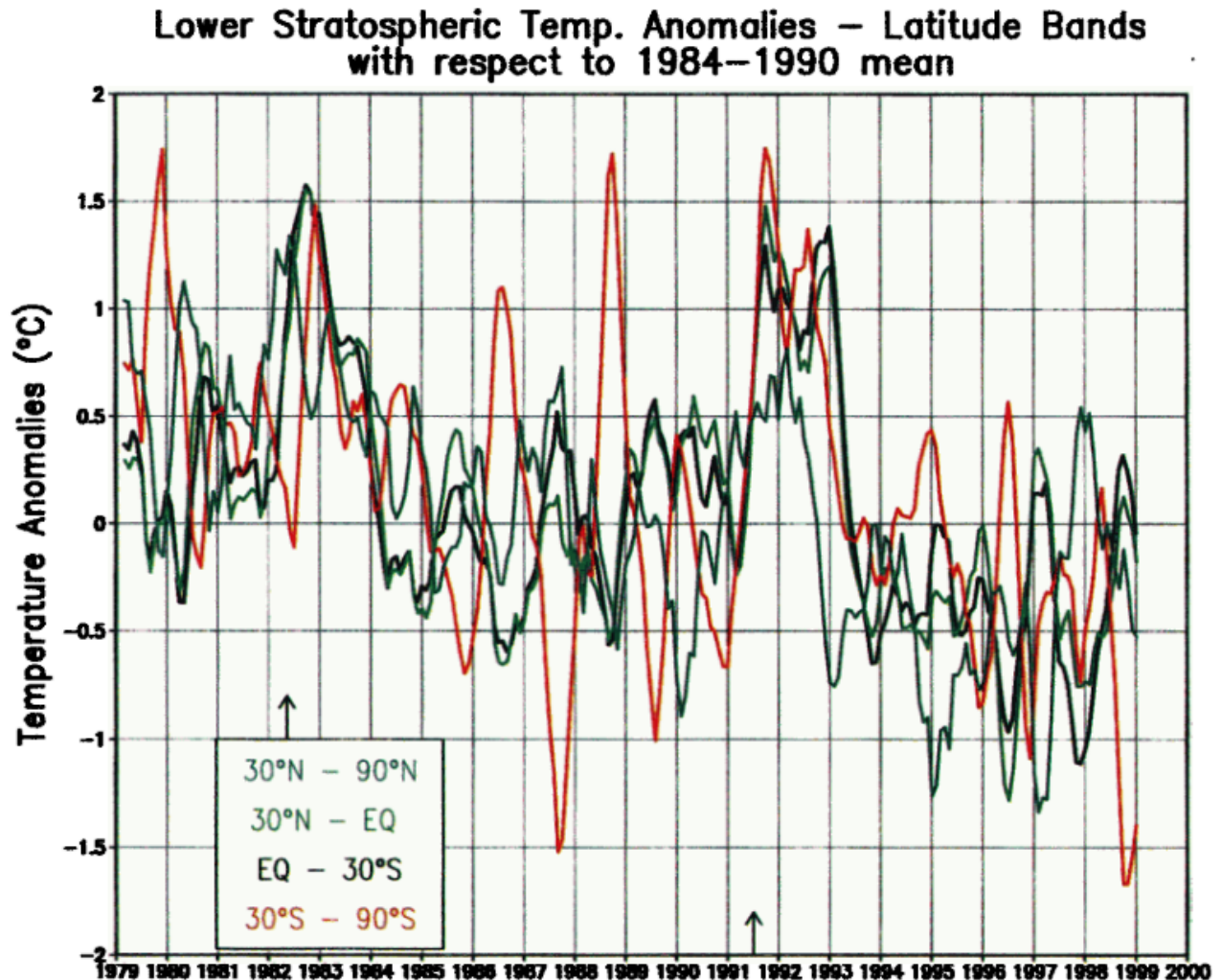


Figure 14: Lower stratospheric temperature anomalies by year and with the latitude bands labeled (Robock, 2000).



PART 2: The Model Comparison

Chapter 3: Model Descriptions

Researchers have spent almost 2 decades developing solar radiation management models. The GeoMIP scenarios are standardized guidelines for setting up geoengineering experiments. These guidelines make it easier to compare model results. The paper *Impacts, effectiveness and regional inequalities of the GeoMIP G1 to G4 solar radiation management scenarios* published in 2015 with the primary author Xiaoyong Yu compares the results of many different climate models for the same GeoMIP experiment. This paper explores the regional temperature and precipitation changes at the global, regional, and grid level.

Section 1: The Geoengineering Intercomparison Project (GeoMIP)

The GeoMIP guidelines developed by Kravitz in 2010 and 2011 outline specifications for designing geoengineering experiments. The purpose of creating the GeoMIP experiment scenarios was to standardize geoengineering models so that they could be compared. Prior to development, models fluctuated in results not only due to variations within the models but also due to differing starting conditions and methods for setting up geoengineering simulations. After development, researchers interested in studying geoengineering using different models had a standardized experiment setup. Researchers from different groups can study and compare the results using this standard.

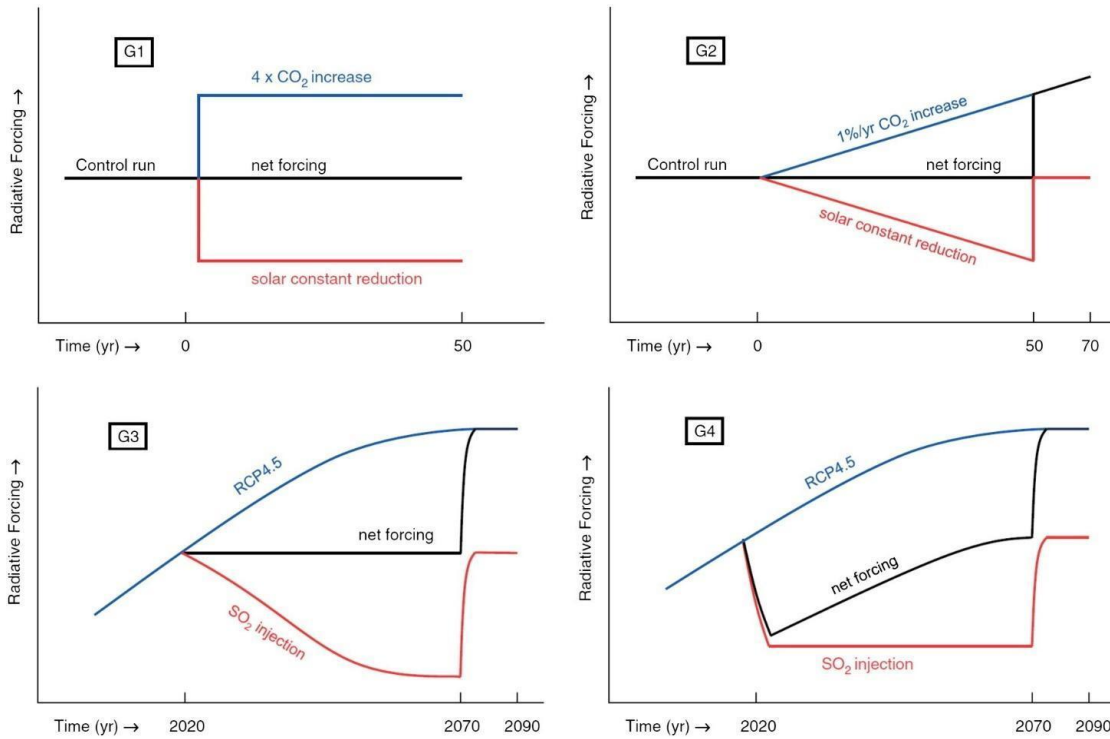
Each GeoMIP scenario consists of a control reference period for the climate conditions before any geoengineering occurs. For each scenario, geoengineering is

applied during a specific time interval to combat a specific CO₂ emission case. These control and climate change experiments utilized a preindustrial control run, abrupt quadrupled CO₂, 1% per year CO₂ increase, and RCP4.5 (Representative Concentration Pathway at 4.5 W/m²). The preindustrial control run (piControl) has all concentrations of gasses, emissions, and short-lived reactive species at pre-industrial climate levels. The land use is also fixed at a preindustrial level. The abrupt 4xCO₂ experiment begins with piControl before quadrupling the CO₂ concentration. The 1% CO₂ experiment begins at preindustrial levels and then increases the CO₂ concentration at 1% per year until the levels are at four times the pre-industrial level. The RCP4.5 experiment means that all emissions and concentration are such that radiative forcing over time is stabilized to 4.5 W/m² by the year 2100 starting in the year 2000. This is a continuation of the historical run (Kravitz et al., 2010).

The GeoMIP scenarios are labeled G1, G2, G3, G3S, and G4 and build upon the experiments described above. The G1 experiment, shown in Figure 15, starts with a piControl run. At the beginning of the experiment, CO₂ levels instantaneously quadruple from pre industrial levels. The model reduces the solar constant so that net forcing is unchanged from the control run. This experiment is performed so that in subsequent scenarios the climate response to radiative forcing from CO₂ will have a high signal to noise ratio, meaning that it will be accurate and tuned to the model being used. In G1, the experiment balances global average radiative forcing by reducing the solar constant. Simple calculations using the global average planetary albedo obtain a reduction in the solar constant. Researchers make corrections after a few years of simulation and restart the model using these corrections. The model used will determine the solar constant

change needed as CO₂ radiative forcing and planetary albedo may differ between models. This tuning procedure is therefore necessary as it determines the change in solar constant for the specific model used. This value is important for the G2 experiment (Kravitz et al., 2011).

Figure 15: GeoMIP G1 through G4 scenarios (Yu et al., 2015).



Equation 1: Radiative forcing and solar constant, α refers to the planetary albedo (Kravitz et al., 2010).

$$\Delta RF = \frac{S_0}{4} (1 - \alpha)$$

In the first step for running the G1 experiment, researchers evaluate the steady state net radiation (TOA) difference between 4xCO₂ and the preindustrial control. In the next step, research groups evaluate Equation 1 by setting ΔRF equal to the value from the first step and then solve for S_0 . Following this calculation, the research group runs a ten-year G1 run with the CMIP5 (Coupled Model Intercomparison Project Phase 5)

$4\times\text{CO}_2$ experiment. The model reduces the solar constant by the value found in the previous step. Finally, the model evaluates the TOA from the previous step and if the TOA is less than a 0.1 W/m^2 difference from that of the control run then the experiment continues. If this is not true, researchers adjust the solar constant and repeat step 3. The 10-year period is important because past simulations have shown that if the model is balanced for the initial 10 to 15 years, it will remain balanced for the 50 remaining years of the experiment (Kravitz et al., 2010).

The G2 experiment is shown in Figure 15 and is similar to the G1 experiment in that it balances the net forcing through a reduction in solar constant to counteract the additional forcing due to an increase in CO_2 . Unlike in the G1 experiment, where the CO_2 levels were instantly quadrupled, the CO_2 levels increase at 1% per year, starting from the same control run. The CO_2 is exponentially increasing so the radiative forcing scales with a logarithm of CO_2 concentration and is a straight line as shown in Figure 15. In addition, the solar constant as shown is linearly decreased over time. The scaling for the solar constant change is found using the results from the G1 experiment (Kravitz et al., 2011).

The steps for the G2 experiment depend on the value obtained in G1 for the reduction in solar constant. From this value, researchers estimate the linear reduction in solar constant. The radiative forcing increases as the log of the concentration so the solar constant should decrease linearly. After this estimate, groups perform a 10-year G2 run using this slope. Again if the TOA is within a 0.1 W/m^2 difference of the control run, researchers should continue with the experiment. If not, groups adjust the values, and then repeat the previous step. Past experimentation has shown that any temperature variations in G2 will be small until simulation year 20 (Kravitz et al., 2010).

The G4 scenario also has an aerosol layer, with aerosols injected into the atmosphere at a constant annual rate. This annual rate will begin in 2020. This model is especially useful as the injection rate does not depend on the model transforming emission rates into concentration and can give insight into the uncertainties that emerge in models due to this conversion. For this scenario, GeoMIP recommends the injection rate at 5 Tg SO₂ per year. This recommendation is on the maximum end of a range of injection rates that research determined would offset a doubling of CO₂ concentration and reduce temperatures to 1980s levels. GeoMIP chooses the larger end of the range to maximize signal to noise ratio for the climate response to geoengineering. As can be seen in Figure 15, geoengineering stops for G3 and G4 in 2070, after which the net forcing jumps to the RCP4.5 level. GeoMIP recommends that the model extend 20 years after SO₂ injection stops to study the climate response (Kravitz et al., 2011).

The G3 experiment is like G2 but provides a more realistic scenario for the implementation of stratospheric geoengineering. The G3 experiment, shown in Figure 15, assumes a RCP4.5 scenario. G3 starts with RCP4.5 until the year 2020 after which the model adds stratospheric aerosols gradually to balance the CO₂ forcing. The balancing is such that the planetary temperature is as near to constant as allowed by the model limitations. This will require different amounts of aerosols at different times to achieve radiative balance. In an ideal model, it adds the sulfate from an equatorial injection location of SO₂ and will create, grow, and transport the aerosol from the original injection site. If this is not possible due to model limitations on transport of the aerosol, the model should add aerosols at the equator or globally in a similar manner to the way the model would treat volcanic aerosols. Ideally, the model should include ozone (O₃) chemistry,

carbon cycle, and coupling with physical climate systems. This will allow the exploration of additional impacts of the aerosols. For the carbon cycle, the model should be run in concentration rather than emission driven mode. It is recommended that the model run G4 before G3 due to values from G4 better informing the G3 experiment (Kravitz et al., 2011).

Researchers use the results from the G4 experiment to estimate sulfate aerosol radiative forcing for SO₂ injections. The amount of sulfate aerosol needed to balance greenhouse gas forcing is estimated. These estimates are difficult to estimate accurately therefore the desired 0.1 W/m² tolerance may not be achievable. The G3S experiment which is optional may make this estimation process easier and more accurate (Kravitz et al., 2010).

The G3S experiment is optional in the GeoMIP suite but useful in understanding radiative forcing in the modern climate. The experiment is conducted in the same manner as the G3 experiment but instead of using sulfate aerosols to counteract the increase in greenhouse gas radiative forcing, the model obtains the balance through a reduction in the solar constant. Without the inclusion of G3S, there is no experiment which determines the reduction in solar constant in combination with a present-day climate. This experiment is an extension of the G2 experiment except that it deals with a reduction in the solar constant in a modern climate as opposed to pre-industrial climate. Climate, chemistry, land surface, and feedback mechanisms in the modern climate are different from the pre industrial climate.

In the steps for the experiment, researchers calculate the values for anthropogenic radiative forcing for the reference scenario RCP4.5 and calculate S₀ using Equation 1 and

averaging over the period between 2010 and 2030. They then subtract this number from the values calculated for the year 2020 and reduce the solar constant by this number. Unlike in the previous experiments, the radiative balance using this method may not be within a 0.1 W/m^2 threshold (Kravitz et al., 2010).

Section 2: The Climate Models Used

The authors of the Yu2015 paper's determine the effectiveness of solar radiation management (SRM) in mitigating changes in temperature and precipitation on global and regional scales due to increase in greenhouse gas concentrations. The paper used various Earth System Models to examine surface air temperature and precipitation changes due to the GeoMIP experiments. Table 5 gives the models used in the paper. Not all models could perform all GeoMIP experiments. Table 6 gives the number of models that the authors used to model each scenario. It also gives the year range they used for modeling. The no SRM terms are the control runs. They obtained these scenarios from the Coupled Model Intercomparison Project (CMIP5) which modeled the pre-industrial control, the 4xCO₂, and the RCP4.5 scenarios.

Table 5: Model used by the paper for each GeoMIP experiment. It should be noted that there were originally 4 models in total that completed G3 but GISS-E2-R was excluded from analysis (Yu et al., 2015).

<i>Model</i>	<i>G1</i>	<i>G2</i>	<i>G3</i>	<i>G4</i>
<i>BNU-ESM</i>	X	X	X	X
<i>CanESM2</i>	X	X		X
<i>CESM-CAMS5.1-FV</i>	X			
<i>CCSM4</i>	X	X		
<i>CSIRO Mk3L</i>	X	X		X
<i>EC-Earth</i>	X			
<i>GISS-E2-R</i>	X	X		X
<i>HadCM3</i>	X	X		
<i>HadGEM2-ES</i>	X	X	X	X
<i>IPSL-CM5A-LR</i>	X		X	
<i>MIROC-ESM</i>				X
<i>MPI-ESM-LR</i>	X	X		
<i>NorESM1-M</i>	X	X		

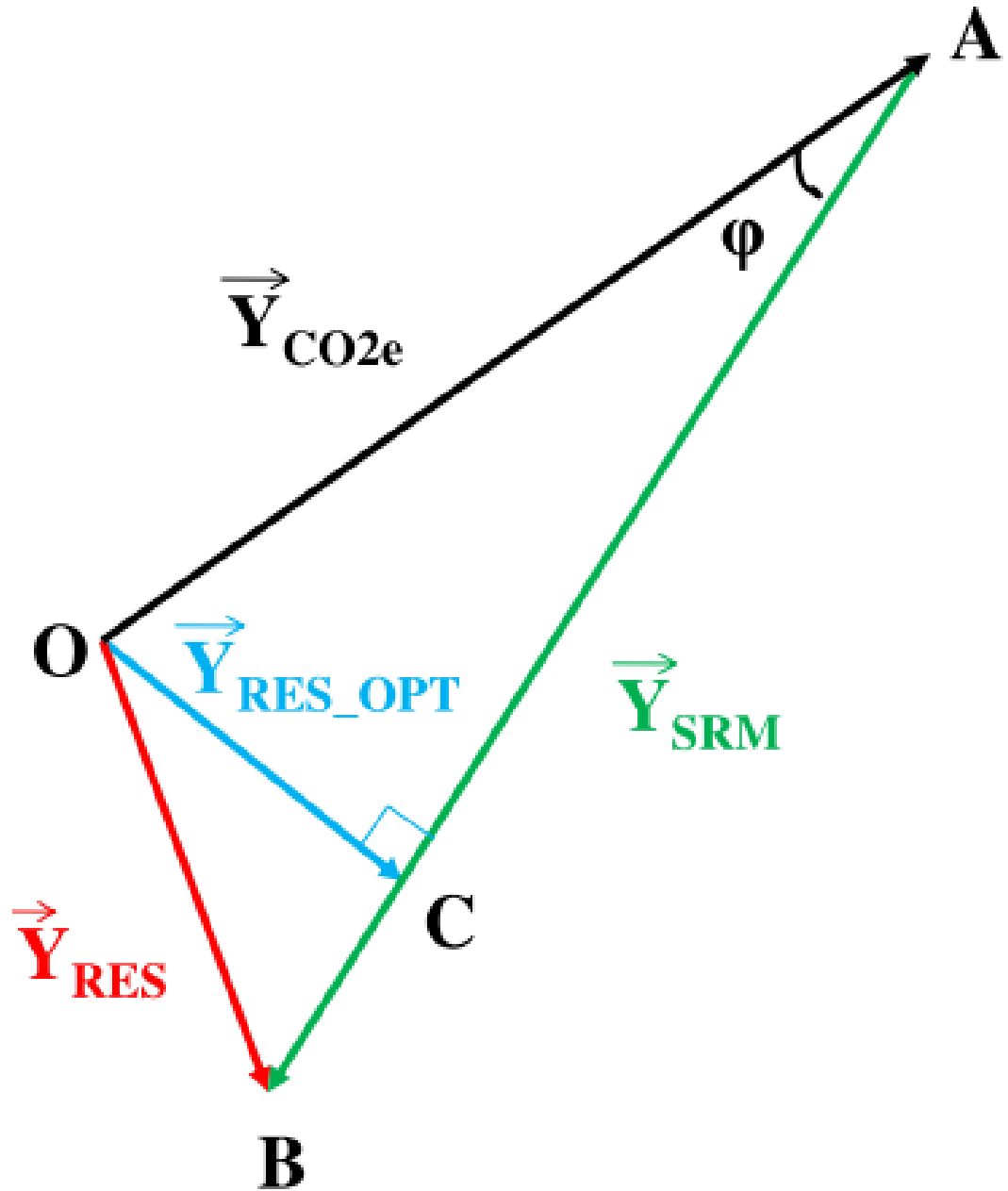
Table 6: Information about each GeoMIP scenario explored in the paper. Each GeoMIP experiment and its baseline climate is listed under the columns SRM and No SRM respectively. The averaging period refers to the year ranges that were used in calculations. The baseline climate is the reference that occurred before any geoengineering and number of models is a count from table 4 for each scenario (Yu et al., 2015).

<i>SRM Experiment</i>	<i>No SRM Experiment</i>	<i>Averaging period</i>	<i>Baseline climate</i>	<i>Number of Models</i>
<i>G1</i>	Abrupt 4xCO ₂	Experiment year 11-50	Pre-industrial average	13
<i>G2</i>	1pct CO ₂	Experiment year 11-50	Pre-industrial average	12
<i>G3</i>	Rcp45	2030-2069	Average over 2010-2029 under rcp45	3
<i>G4</i>	Rcp45	2030-2069	Average over 2010-2029 under rcp45	7

Section 3: The RCR Method (Residual Climate Response)

The models used in the paper to perform the GeoMIP experiments needed a method for balancing the atmospheric changes due to SRM with those due to increased CO₂ concentrations. SRM counteracts increasing radiative forcing due to increased CO₂ concentrations. The process of determining how much aerosol or solar constant reduction to apply to achieve this goal can be accomplished using the Residual Climate Response (RCR) Method. Increasing CO₂ concentrations have a different effect on the regional and local level than they do on the global level. Simply balancing radiative forcing at the global scale would not achieve the desired regional results. The RCR method models the changes due to SRM and CO₂ concentrations for each region as vectors where each component represents a particular regional climate change due to either CO₂ concentrations or SRM. The angle between these two vectors is then representative of the difference between SRM compensated climate change and CO₂ forcing alone. The authors used this angle to find the optimal aerosol levels for geoengineering. In order to apply the RCR, the regional responses have to be approximately linear. Although generally many climate systems variables are nonlinear, the temperature and precipitation model responses are approximately linear (Yu et al., 2015).

Figure 16: a diagram of the RCR approach. The origin O is representative of the reference state of a single climate variable which is denoted as Y. This would be SAT or precipitation for the control climate. The vector \vec{Y}_{CO2e} is the regional changes from the reference state due to CO₂ emissions and each component of the vector represents the change for a given region on the globe. The vectors \vec{Y}_{SRM} and \vec{Y}_{RES} have the same format and correspond to the change compensated for by SRM and the difference between these two vectors respectively. The angles between \vec{Y}_{CO2e} and \vec{Y}_{SRM} are denoted by ϕ which represents the regional inequality in the effectiveness of SRM. The vector \vec{Y}_{RES_OPT} is the vector that optimizes this angle and therefore the regional compensation due to SRM (Yu et al., 2015).



The angle between the \mathbf{Y}_{CO_2e} and \mathbf{Y}_{SRM} communicates the regional inequality in effectiveness. The Yu2015 paper found this using Equation 2.

Equation 2: Regional inequality in effectiveness (Yu et al., 2015).

$$\varphi = \left(\frac{-\mathbf{Y}_{CO_2e} \cdot \mathbf{Y}_{SRM}}{\|\mathbf{Y}_{CO_2e}\| \|\mathbf{Y}_{SRM}\|} \right)$$

The damages due to CO₂ emission are defined as being proportionate to the square of the regional change which gives the following formula for the percentage of damages compensated by SRM. This is the actual effectiveness of a solar radiation management strategy Equation 3.

Equation 3: The actual effectiveness of SRM (Yu et al., 2015)

$$\left(1 - \frac{\|\mathbf{Y}_{RES}\|^2}{\|\mathbf{Y}_{CO_2e}\|^2} \right) \times 100\%$$

The model uses this to find the optimal effectiveness for a particular SRM scenario and angle φ . This is expressed by Equation 4.

Equation 4: Optimal effectiveness (Yu et al., 2015)

$$\left(1 - \frac{\|\mathbf{Y}_{RES-OPT}\|^2}{\|\mathbf{Y}_{CO_2e}\|^2} \right) \times 100\% = (1 - \sin^2 \varphi) \times 100\%$$

An effectiveness of 100% would mean that SRM is compensating for all the change in the climate variable while a negative effectiveness means that SRM increases the change in \mathbf{Y} . The paper used the adjustment percentage for the SRM compensated change to obtain the optimal compensation effectiveness for \mathbf{Y} . They calculated this using Equation 5.

Equation 5: Optimal compensation effectiveness (Yu et al., 2015)

$$\left(\frac{\|Y_{CO_2}\| * \cos\varphi}{\|Y_{SRM}\|} - 1 \right) \times 100\%$$

The paper chooses the level of SRM that minimizes damages across all regions without making any individual region experience higher damages with SRM than without. This method allows the individual regional responses to be considered when implementing SRM in the model. The paper expands on earlier research using this model by applying the method to all the GeoMIP experiments. They also perform a noise calculation by comparing angles between different trials of the control climates. The angle should be 0 so any deviation from this gives a metric for noise in the model (Yu et al., 2015).

Chapter 4: Procedure

The Climate Data Gateway at NCAR (National Center for Atmospheric Research) has a database for the GeoMIP project which contains model outputs for experiments G1, G2, and G3S. It also has datasets for piControl and Abrupt 4xCO₂. The same website has the CMIP5 (Coupled Model Intercomparison Project Phase 5) data outputs which provides a dataset for the RCP4.5 and 1pctCO₂ scenarios. I processed the data using the R programming language to obtain similar graphs and averages as those found in the Yu2015 paper. The paper analyzed the global weighted average, regional averages, and grid level anomalies maps for the precipitation and surface temperature change for the different scenarios. This chapter focuses on the procedure involved in processing the data from NCAR and calculating the various graphs and averages from the paper.

The paper used the CSSM4 model, but only ran G1 and G2 experiments; it did not run G3S experiments on any model. I used the scenarios to evaluate the agreement between the NCAR data and the paper results. The paper also used the RCR regionalization which was not implemented to produce the NCAR data. I then analyzed the properties of the G3S experiment from the NCAR database. This chapter focuses on the procedure used to obtain the different averages and maps while chapter 5 analyzes the results.

Section 1: NCAR Datasets

The NCAR GeoMIP project data contained only G1, G2, and G3S, Picontrol, and Abrupt 4xCO₂ data. The RCP4.5 and 1pctCO₂ data came from the CIMP5 project. I

collected multiple ensembles outputs for each dataset. Although there were many climate variables to explore, I only downloaded those corresponding to the precipitation and the surface air temperature (SAT). The surface air temperature is the daily average temperature $2m$ above the Earth's surface measured in K . The precipitation flux is the amount of water per unit area per unit time and the units were $kg/(m^2s)$.

The metadata is an array with dimensions of 288 by 192 by whatever the number of months is in the year range for the simulation. The first two dimensions correspond to the spatial longitudinal and latitudinal coordinates and are the same across all datasets. The longitudes have 288 values ranging from 0.00 to 358.75. The latitudes have 192 values and range from -90 to 90. I used the area cell dataset to interpret the area of each spatial coordinate. This dataset has the area in m^2 for each spatial coordinate. Each dataset has its own corresponding area cell dataset, but they are all identical.

To prepare the data for further analysis, I calculated the ensemble average over the period used in the Yu2015 paper. I first took a subset of the time coordinates of the original dataset over the months from the time periods referenced in Table 6. I took the average of all usable ensembles for each time and spatial point. The final arrays containing the metadata for SAT and precipitation are listed in Table 7.

Table 7: Metrics for the ensemble average datasets used in the procedure. The first column lists the experiments while the second column lists the ensembles available for the average. The last two columns reiterate the experiment years also with the final dimensions of the arrays. A separate dataset for each variable SAT and precipitation exists.

<i>Experiment</i>	<i>Ensembles Averaged</i>	<i>Experiment Years</i>	<i>Final Dimensions</i>
<i>G1</i>	1, 2	1861-1900	288 x 192 x 480
<i>piControl</i>	3	1861-1900	288 x 192 x 480
<i>Abrupt4xCO2</i>	4	1861-1900	288 x 192 x 480
<i>G2</i>	2	1861-1900	288 x 192 x 480
<i>1pctCO2</i>	1	1861-1900	288 x 192 x 480
<i>G3S</i>	1, 2, 3	2030-2069	288 x 192 x 480
<i>Rcp45_2010_2029</i>	1, 2, 3, 4, 5, 6	2010-2029	288 x 192 x 240
<i>Rcp45_2030_2069</i>	1, 2, 3, 4, 5, 6	2030-2069	288 x 192 x 480

Section 2: Area Weighted Global Mean Calculation

The area weighted global mean is the average SAT or precipitation change over the entire globe. The different spatial coordinates correspond to different actual areas as the coordinates are mapped on a sphere. The area weighted average must be used to get an accurate global temperature change. The Yu2015 paper calculates the change between the weighted global averages of the climate change scenarios and the reference scenarios. The climate change scenarios G1, Abrupt 4xCO₂, G2, and 1pctCO₂ have reference climate piControl while G3S and RCP4.5_2030_2069 have the reference RCP4.5_2010_2029. I used the same regional averages and the anomalies maps described in further sections. Equation 6 was used to calculate these averages for all desired combinations.

Equation 6: Function for global weighted area mean. The inputs are two arrays (climate change scenario and reference). The function calculates the time average of each array and then the area of each spatial coordinate is multiplied by the grid area. The sum of this value over the sum of the global area is the weighted average for one of the scenarios. Finally, the climate change scenario is subtracted from the reference scenario to find the change.

```
weighted.mean <- function(array1, array2,
  area = area) {
  val <- sum(area * apply(array1, c(1, 2),
    mean))/sum(area) - sum(area * apply(array2,
    c(1, 2), mean))/sum(area)
  return(val)
}
```

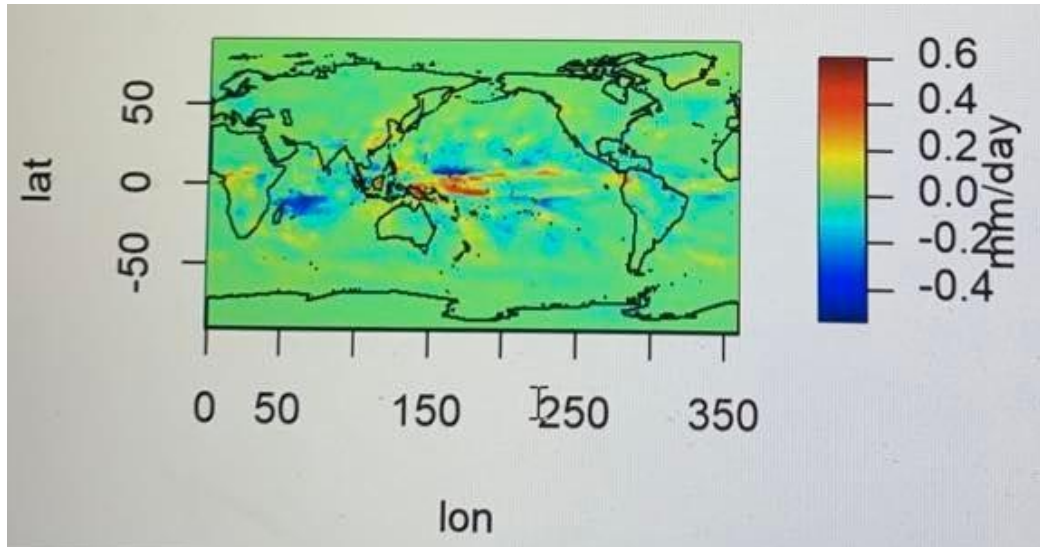
The variable for SAT from the raw data came with units of K so no conversion is needed. The precipitation is in units of $kg/(m^2s)$ and the desired units for comparison with the Yu2015 paper are mm/day . This can be converted by multiplying by the number of seconds in a day which is $86400\ s/day$. I used this conversion to obtain the results for the precipitation variable in all the calculations. The next chapter gives the analysis along with the values obtained in Yu2015.

Section 3: Global Anomalies Graphs and Coordinate Transformation

The global anomalies map shows the difference between the experiment and reference climates at each individual spatial point. I calculated this by taking the time average of each and subtracting the reference scenarios from the experiment scenarios. The difference in the spatial coordinates used in the NCAR data and the typical longitude and latitude coordinates was the difference in the spatial coordinates used in the NCAR data and the typical longitude and latitude coordinates.

To get the traditional orientation of the latitudes and longitudes, the data had to be reoriented. As can be seen in Figure 17, the raw data produced a map centered on the Pacific Ocean with Africa being split at the end and beginning of the map. The longitudes 0 to 180 correspond to the traditional eastern longitudes (0 to 180E) while the longitudes greater than 180 are the western longitudes and are converted to the typical longitude values by subtracting 360. I corrected the longitudes coordinates to correspond to -180 to 180 with the negative values being the western longitudes. The matrix containing the data is also converted by taking the spatial points belonging to longitudes greater than 180 and placing them before the spatial coordinates with values 0 to 180. This transformation creates the traditional map with the image centered around the continents.

Figure 17: Anomalies map of precipitation G3S-RCP4.5_2010_2029 with original longitudes. The longitude range is 0 to 360 causing the map to be centered around the pacific ocean. The Eastern hemisphere is on the left side of the map instead of the right side where it typically is. The western hemisphere is similarly displaced. Transforming the coordinates in the western hemisphere from 180 through 360 to -180 through 0 will center the map on Africa and Europe as is traditional.



Section 4: Regional Area Weighted Averages

Section 2 calculated the global weighted mean change. This section breaks the landmass of the continents into regions with similar climate and geological features and calculates the area weighted mean of each region. I converted the spatial coordinates of the regions to the system used in the NCAR data using the method described in Section 3. Table 8 has the traditional coordinates of the regions as well as the converted coordinates used for the NCAR data. As was done in the paper, a Student's t test is used to determine if the changes were significant. I also calculated the global land mass weighted average

I used Equation 7 and Equation 8 to calculate the regional weighted averages. Equation 7 determines which spatial coordinates belong to which regions. I used these results and Equation 8 to calculate the mean for each region. Equation 8 only returned a single region so I repeated the function in a loop to create a dataframe of regional mean values. The results are in Chapter 5.

Table 8: Region Coordinates and regions used in the calculations (Giorgi & Francisco, 2000) and (Christensen et al., 2007). The region names and acronyms are given as well as the latitude and longitude coordinates. The 2000 paper did not split Northern Australia and Southern Australia while the Yu 2015 paper did make that distinction. The 2007 paper gives the coordinates for this split. The last columns list the transformed latitude and longitudes based on the spatial coordinates used in the NCAR data.

<i>Name</i>	<i>Acronym</i>	<i>Latitude</i>	<i>Longitude</i>	<i>Transformed Latitude</i>	<i>Transformed Longitude</i>
<i>Northern Australia</i>	NAU	30S – 11S	110E – 155E	-30 – -11	110 – 155
<i>Southern Australia</i>	SAU	45S – 30S	110E – 155E	-45 – -30	110 – 155
<i>Amazon Basin</i>	AMZ	20S – 12N	82W – 34W	-20 – 12	278 – 326
<i>Southern South America</i>	SSA	56S – 20S	76W – 40W	-56 – -20	284 – 320
<i>Central America</i>	CAM	10N – 30N	116W – 83W	10 – 30	244 – 277
<i>Western North America</i>	WNA	30N – 60N	130W – 103W	30 – 60	230 – 257
<i>Central North America</i>	CAN	30N – 50N	103W – 85W	30 – 50	257 – 275
<i>Eastern North America</i>	ENA	25N – 50N	85W – 60W	25 – 50	275 – 300
<i>Alaska</i>	ALA	60N – 72N	170W – 103W	60 – 70	190 – 257
<i>Greenland</i>	GRL	50N – 85N	103W – 10W	50 – 85	257 – 350
<i>Mediterranean Basin</i>	MED	30N – 48N	10W – 40E	30 – 48	350 – 40
<i>Northern Europe</i>	NEU	48N – 75N	10W – 40E	48 – 75	350 – 40
<i>Western Africa</i>	WAF	12S – 18N	20W – 22E	12 – 18	340 – 22
<i>Eastern Africa</i>	EAF	12S – 18N	22E – 52E	-12 – 18	22 – 52
<i>Southern Africa</i>	SAF	35S – 12S	10W – 52E	-35 – -12	350 – 52
<i>Sahara</i>	SAH	18N – 30N	20W – 65E	18 – 30	340 – 65
<i>Southeast Asia</i>	SEA	11S – 20N	95E – 155E	-11 – 20	95 – 155
<i>East Asia</i>	EAS	20N – 50N	100E – 145E	20 – 50	100 – 145
<i>South Asia</i>	SAS	5N – 30N	65E – 100E	5 – 30	65 – 100
<i>Central Asia</i>	CAS	30N – 50N	40E – 75E	30 – 50	40 – 75
<i>Tibet</i>	TIB	30N – 50N	75E – 100E	30 – 50	75 – 100
<i>North Asia</i>	NAS	50N – 70N	40E – 180E	50 – 70	40-180

Equation 7: Function to subset for each region. The output of this function is a list of true/false values that indicate which spatial coordinates to include for each region. The if/else statement is needed since regions in the west occur at the end and the beginning of the array whereas regions in the east are coordinates between the given range.

```
coor.bounds <- function(df.r) {
  if(df.r[[3]] > df.r[[4]]) {
    lon.b <- (df.r[[3]] < lon) | (lon <
df.r[[4]])
  } else {
    lon.b <- (df.r[[3]] < lon) & (lon <
df.r[[4]])
  }
  lat.b <- (df.r[[1]] < lat) & (lat <
df.r[[2]])
  return(list(lon.b, lat.b))
}

coor_bounds <- apply(df.regions, 1,
coor.bounds)
```

Equation 8: Function for calculating the regional weighted averages based on bounds inputs. The inputs are two arrays for the climate change and the reference scenarios and the bounds calculated using equation 7. The bound input is one element of the list or region. The bounds are used to subset the area array and the two input arrays. Then the weighted average is calculated in the same manner as equation 6.

```

`regional.mean <- function(array1, array2,
bounds) {
  # assume the spatial coordinates are
  # consistent
  a <- area[bounds[[1]], bounds[[2]]]
  v1 <- (a * apply(array1, c(1, 2),
  mean)[bounds[[1]], bounds[[2]]]) / sum(a)
  v2 <- (a * apply(array2, c(1, 2),
  mean)[bounds[[1]], bounds[[2]]]) / sum(a)
  val <- sum(v1) - sum(v2)
  return(val)
}
`
```

The Yu2015 paper performs a Student's t test on the regions to determine whether the change is significant at a 95% confidence level. Equation 9 performs this calculation for each region and looping through this function results in a dataframe containing the p values. Rejecting the null hypothesis means that the means have a statistically significant difference. It should be noted that this test also depends on the number of data points or pairs of spatial coordinates available and not just the size of the difference in means. This means that the difference in means can be smaller and still be statistically significant for a larger region with more spatial points than a smaller region. Using the regional changes, I calculated the average land mass change as the area weighted average of the 22 regions. I also performed a Student's t test for the land mass average. These results are also included in Chapter 5.

Equation 9: Function for regional Student's t test. The function used the area weighted mean in the t.test function. This is done by multiplying each spatial coordinate by the corresponding area and then divided by the total area. The traditional average of this vector gives the weighted average. The t test is done at a 95% confidence interval and the null hypothesis (not significant difference in means) is rejected for p values less than 0.05.

```
regional.t.test <- function(array1, array2,
bounds) {
  a <- area[ bounds[[1]], bounds[[2]] ]
  v1 <- (a * apply(array1, c(1, 2),
mean) [bounds[[1]], bounds[[2]]])/sum(a)
  v2 <- (a * apply(array2, c(1, 2),
mean) [bounds[[1]], bounds[[2]]])/sum(a)
  t_test <- t.test(as.vector(v1) *
prod(dim(v1)),as.vector(v2)*prod(dim(v2)),
alternative = "two.sided")
  return(t_test$p.value)
}
```

Chapter 5: Results and Discussion

This chapter analyzes and compares the results from the Yu2015 paper and the NCAR data. This paragraph gives an overview of the results for the global, regional, and grid level. The conclusion also gives an overview of the results. The global average SAT and precipitation changes from the NCAR data are within a standard deviation of the Yu2015 results for the overlapping climate scenarios. The G3S - RCP4.5_2010_2029 global mean is close to 0 for both precipitation and SAT, which is expected, and indicates the model is operating as intended. The NCAR data and the Yu2015 have the largest SAT regional changes occurring in Alaska, Greenland, Northern Europe, and North Asia. There is high disagreement between models in the Yu2015 results for the grid level changes. The NCAR data generally agrees with Yu2015 in finding the largest temperature changes at the poles and the smallest changes over the oceans, but the high uncertainty makes comparison for the continents difficult. The NCAR and YU2015 data agree that precipitation changes at the equator were more extreme and alternate between decreasing and increasing.

Section 1: Global Area Weighted Mean Results

Table 9 shows the area weighted global averages for the NCAR data and the Yu2015 results. For overlapping results between the two, the change in temperature and precipitation from NCAR is within the standard deviation of the Yu2015 results. The global averages from NCAR agree with the Yu2015 paper results for SAT and precipitation. The precipitation results are particularly close to the Yu2015 average results; they agree in sign and are only a few hundredths of a decimal off. The SAT

values do not as closely match the Yu2015 results. The change from the G1 and G2 experiment is greater than the Yu2015 results while the increasing CO₂ climate concentration scenarios have less of a change in temperature.

The G3S experiment reduced the radiative forcing constant to account for the modern RCP4.5 climate. The experiment yielded a temperature change close to 0, which is expected as the model balances the increasing radiative forcing due to increased CO₂ concentration with a decrease in the solar constant. The precipitation change was a very small negative number.

For the Yu2015 SAT results, the G1 and G2 are very close to 0 while the G3 and G4 are close in value even though the G3 scenario was intended to mitigate all anthropogenic warming. Both G4 and G3 have a positive temperature change although the standard deviation, which includes 0 and negative temperature change, indicates that statistically the results were close to 0. The G3 scenario was slightly more effective in reducing temperature change than G4. It seems that geoengineering would likely not mitigate all anthropogenic climate changes but compared with the change from the CO₂ concentration scenarios it would have a large noticeable reduction.

Summary

The key takeaways from examining the global average results from both sources are that a decrease in radiative forcing was successfully able to counteract an increase in CO₂ along the RCP4.5 pathway and although geoengineering scenarios G3 and G4 are not able to entirely counteract increased temperatures they are an effective mitigation

strategy. The precipitation results are very close between the NCAR and Yu2015 data and indicate that increasing CO₂ concentrations and radiative forcing increases global precipitation and decreasing radiative forcing decreases precipitation.

Table 9: Global area weighted average for NCAR data and Yu2015 paper. The first two columns are the NCAR data results. The last two columns are from the Yu2015 results and the plus/minus indicates standard deviations in the results.

<i>Experiment</i>	ΔT (°C)	ΔP (mm/day)	ΔT (°C) (Yu et al., 2015)	ΔP (mm/day) (Yu et al., 2015)
<i>G1 - piControl</i>	0.16	-0.14	0.05 ± 0.25	-0.128 ± 0.043
<i>Abrupt4xCO2 -piControl</i>	3.74	0.14	4.30 ± 0.75	0.152 ± 0.055
<i>G2 - piControl</i>	0.23	-0.01	0.07 ± 0.20	-0.020 ± 0.010
<i>1pct - piControl</i>	0.67	0.02	0.71 ± 0.15	0.023 ± 0.006
<i>G3S - rcp45_2010_2029</i>	0.11	-0.01		
<i>G3 - rcp45_2010_2029</i>			0.23 ± 0.28	0.000 ± 0.019
<i>G4 - rcp45_2010_2029</i>			0.28 ± 0.31	0.001 ± 0.025
<i>rcp452030 2069 - rcp452010_2029</i>	0.62	0.03	0.81 ± 0.21	0.043 ± 0.018

Section 2: Regional Area Weighted Mean Results

The Yu2015 paper used bar graphs to represent the changes between the different regions. To compare with the NCAR regional averages, I created similar graphs and also included tables with the exact values. This section is broken down into 4 subsections. The first two are the Yu2015 and NCAR results for SAT and the last two are the Yu2015 and NCAR results for precipitation.

Surface Air Temperature (Yu2015) Results

Figure 18 highlights the regional change results from the Yu2015 paper. For Abrupt 4xCO₂ – piControl, the region with the largest warming is Alaska followed by North Asia and Greenland. Southeast Asia, Southern South American, and Southern

Australia had the smallest change in temperature. The global average over all the regions appears to be about 5 °C and the authors found that all regions are significant by the t test. For G1 – piControl, North Asia, Alaska, Greenland, and Northern Europe have the largest positive temperature change and are all significant. Both Northern Australia and South Asia have significant negative temperature changes. The Abrupt 4xCO₂ shows the most dramatic changes as concentrations are instantly quadrupled and because of this it makes sense that this scenario has the largest temperature changes across regions. This is also true for the global average.

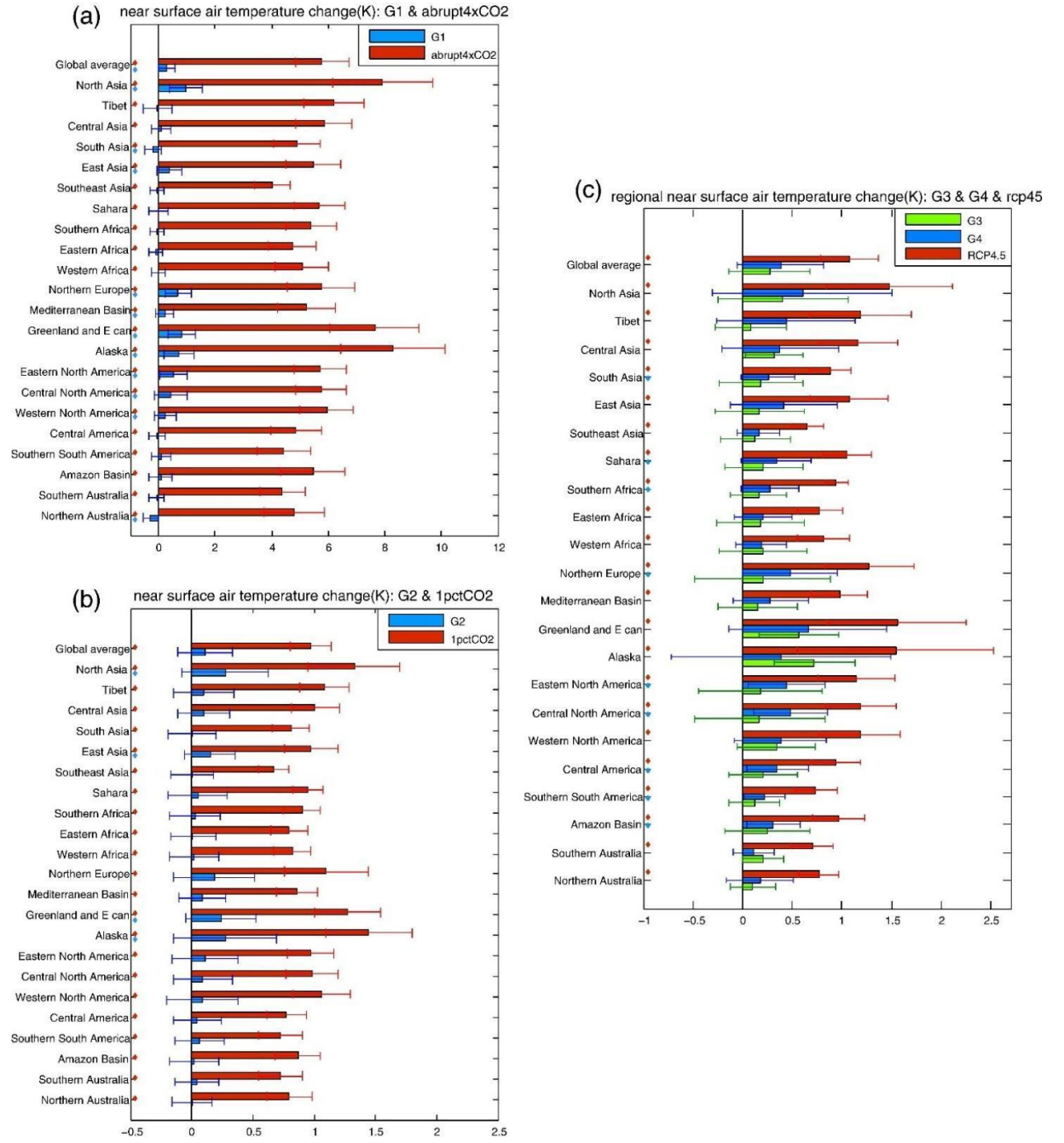
For 1pctCO₂ – piControl, the largest positive temperature change again occurs in Alaska, North Asia, and Greenland. The smallest temperature changes occur in Southern South America, Central America, Eastern Africa, and Western Africa. All changes are significant and the global average across the regions is about 1 °C. For G2 – piControl, the only significant changes are in North Asia, East Asia, Greenland, and Alaska with North Asia and Alaska having the largest change. The global average change was not significant. The temperature changes for G2 are less extreme than those for G1. It is likely that G2 was better able to counteract increased radiative forcing than G1 due to the gradual increase in CO₂ concentration.

For RCP4.5_2030_2069 – RCP4.5_2010_2029, the largest regional changes are in Greenland, Alaska, and North Asia. The regions that experienced the smallest changes are Southeast Asia, Southern Australia, and Southern South America although all changes are significant. This scenario is considered a realistic estimate of a future climate for which increased CO₂ concentrations increase land mass temperature by an average of 1 °C. For G3 – RCP4.5_2010_2029, none of the regions have significant

changes, including the global regional average. This indicates that the G3 scenario was able to counteract increased radiative forcing for all continental land areas. The global average for this scenario was positive but this is likely due to the increase in temperature at the Poles (shown in later sections) which is not accounted for in the regional results. For G4 – RCP4.5_2010_2029, all significant changes are positive with the largest occurring in Northern Europe. This is not unexpected as the G4 scenario injected a fixed amount of aerosol into the stratosphere yearly and was not designed to fully counteract increased radiative forcing.

Overall, G1 has the only significant land average change while the only geoengineering scenario expected to have a positive change is G4. The G4 experiment used a constant injection of aerosols as opposed to the other scenarios which balanced the increased radiative forcing entirely. The regions that consistently experienced the most warming across all scenarios are Alaska, Greenland, Northern Europe, and North Asia.

Figure 18: Regional SAT changes where a diamond indicates whether the change passed a t test (Yu et al., 2015). The red bars indicate values for the increased CO₂ concentration scenarios while green and blue indicate the geoengineering experiments. Figure (a) and figure (b) correspond to reference scenario piControl and Figure (c) corresponds to reference scenario RCP4.5_2010_2029 (Yu et al., 2015).



Surface Air Temperature (NCAR) Results

Figure 19 and Table 10 show the regional SAT results. Figure 19 gives a visual for regional change comparison while Table 9 contains exact values. The only regions for Abrupt 4xCO₂ – piControl that were not significant are Tibet, Northern Europe, Greenland, Eastern North America, Western North America, and Southern South America. The regions Tibet, Greenland and Western North America likely did not pass the significance test due to the limited data points provided in the data and not due to the magnitude of the temperature difference. The sample size issue is due to a combination of the limited spatial coordinates and smaller sizes of the regions. For G1 – piControl, none of the temperature changes are significant. This indicates a true mean of 0 which is the expected result for G1. This is different from the Yu2015 paper which found a significant positive temperature change for G1 – piControl. The significant global regional average for Abrupt 4xCO₂ – piControl is 3.46 °C.

Figure 19(a) has the same regions with the largest SAT change as in the Yu2015 results. For the NCAR data, the smallest changes occurred in Southeast Asia, Central America, and South Africa. There are less significant regions in the NCAR data than there are in the Yu2015 results, but this is likely due to the limited number of spatial coordinates given in the metadata.

The global regional average for 1pctCO₂ – piControl is significant and has a value of 0.53 °C. The only significant local regional changes occur in Southeast Asia, Eastern Africa, Western Africa, and the Amazon Basin. The global regional average for G2 – piControl is also significant and has a value of 0.22 °C. None of the local regional changes are significant. Figure 19(b) gives a very similar pattern of regional averages as

the results from Yu2015; the regions associated with the min and max values are the same for both 1pctCO₂ – piControl and G2 – piControl. The greatest difference in the results appears to be in the relative temperature difference between 1pctCO₂ – piControl and G2 – piControl which has a wider temperature gap for the Yu2015 results. The NCAR data appears to have temperature changes that are closer together with the 1pctCO₂ – piControl changes being smaller than in the paper and the G2 – piControl changes being larger. There were likely models in the Yu2015 results that were highly sensitive to increasing CO₂ concentrations that caused the average of the models to rise.

The global region average temperature change for the RCP4.5_2030_2069 – RCP4.5_2010_2029 is significant and has a value of 0.55 °C. The other significant regional changes occur in Southeast Asia, Eastern Africa, Western Africa, and the Amazon Basin. None of the temperature changes calculated for G3S are significant and they are all below 0.30 °C. This is an expected result since the G3S scenario balances increasing CO₂ concentrations with a decrease in the solar constant. This reduction should fully account for the increased radiative forcing due to the increased CO₂ concentrations. The CCSM4 model used in the NCAR data is able to calculate the decrease in radiation forcing needed to counteract the increase due to the RCP4.5 climate pathway.

For RCP4.5_2030_2069 – RCP4.5_2010_2029, the global regional average is almost half the value of that found in the paper and the other temperature bars are similarly less than those found in the paper. The G3S – RCP4.5_2010_2029 experiment was not in the paper. The area with the largest changes were Alaska, Greenland, North

Asia, and Northern Europe. The smallest changes occurred in Southeast Asia, South Africa, and Western Africa. These results are like the G1 and G2 experimental results.

All models and experiments including the paper results as well as the NCAR results found the largest positive temperature changes occurring in Alaska, Greenland, North Asia, and Northern Europe. This remained true for the G1, G2, G3S, G3, and G4 scenarios although these scenarios still reduced the changes in these areas. The volcanic eruptions research also indicates that the Northern Hemisphere experienced greater climate variability from aerosol injection so this result is not surprising. Additionally, the paper attributes the pattern of increased warming near the poles and decreased warming near the equator as being a result of the balancing of longwave greenhouse gas forcing by shortwave forcing which varies with the season and latitude (Yu et al., 2015).

Figure 19: NCAR Results for regional SAT. Figure (a) is Abrupt 4xCO₂ - piControl and G1 - piControl. Figure (b) is 1pctCO₂ - piControl and G2 - piControl. Figure (c) is RCP4.5_2030_2069 - RCP4.5_2010_2029 and G3S - RCP4.5_2010_2029. The black dots indicate that the regions passed a t test and the change is significant. The purple dots indicate that the change was not significant.

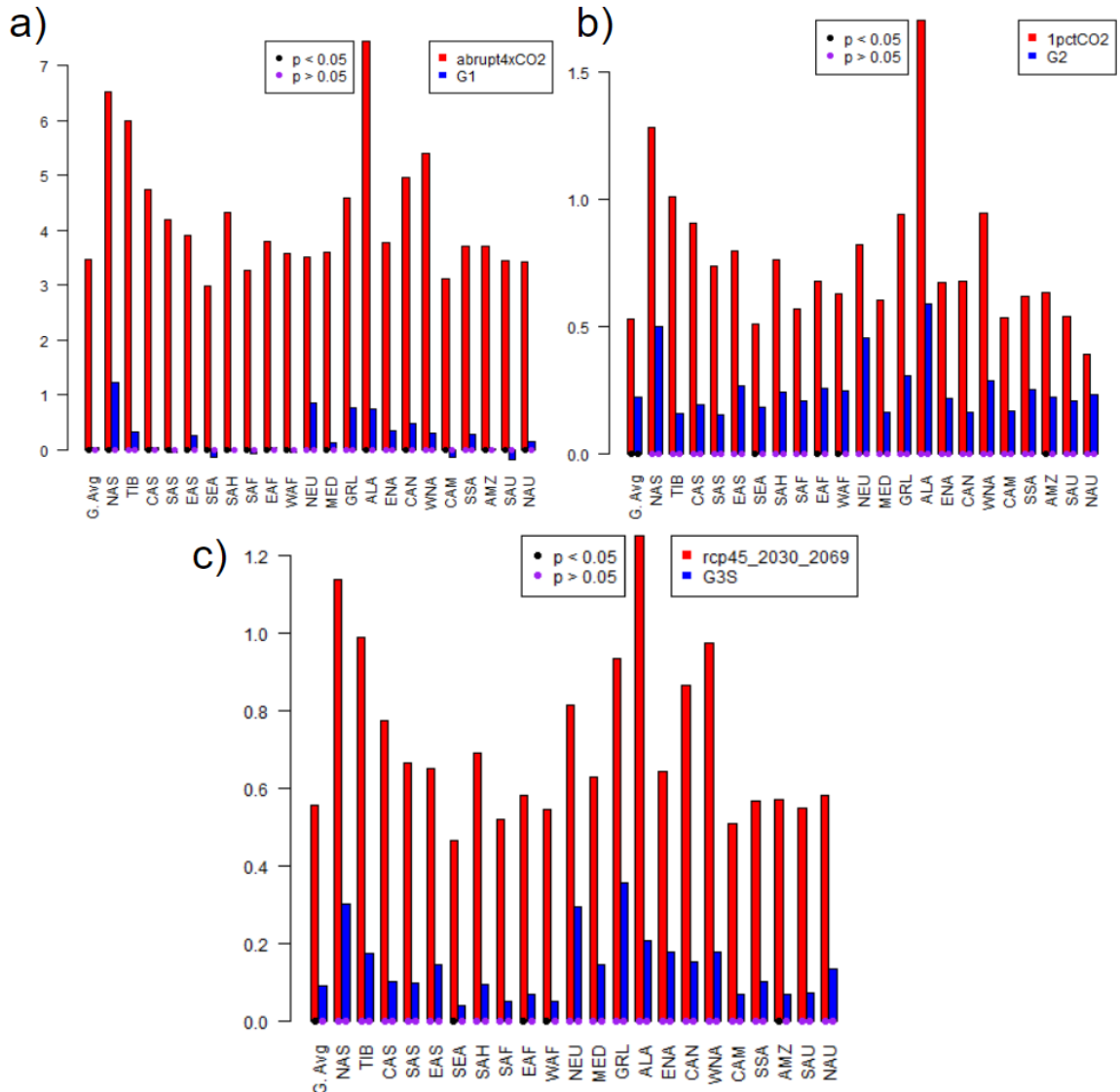


Table 10: Regional SAT changes. The reference climate for the first 4 scenarios is piControl and for the last two it is RCP4.5_2010_2029. A star (*) next to the value in the table indicates that it passed the t test.

Region	Abrupt4xCO ₂	G1	1pctCO ₂	G2	RCP4.5	2030	2069	G3S
<i>Global Average</i>	3.46*	0.04	0.53*	0.22*	0.55*			0.09
<i>North Asia</i>	6.52*	1.22	1.28	0.50	1.14			0.30
<i>Tibet</i>	5.99	0.32	1.01	0.15	0.99			0.17
<i>Central Asia</i>	4.73*	0.04	0.90	0.19	0.78			0.10
<i>South Asia</i>	4.18*	-0.05	0.74	0.15	0.66			0.10
<i>East Asia</i>	3.91*	0.26	0.79	0.27	0.65			0.15
<i>Southeast Asia</i>	2.98*	-0.14	0.51*	0.18	0.47*			0.04
<i>Sahara</i>	4.32*	-0.02	0.76	0.24	0.69			0.09
<i>Southern Africa</i>	3.27*	-0.07	0.57	0.20	0.52			0.05
<i>Eastern Africa</i>	3.80*	0.04	0.68*	0.26	0.58*			0.07
<i>Western Africa</i>	3.57*	-0.06	0.63*	0.25	0.54*			0.05
<i>Northern Europe</i>	3.50	0.85	0.82	0.45	0.82			0.29
<i>Mediterranean Basin</i>	3.59*	0.13	0.60	0.16	0.63			0.14
<i>Greenland</i>	4.58	0.75	0.94	0.31	0.94			0.35
<i>Alaska</i>	7.45*	0.73	1.70	0.59	1.25			0.21
<i>Eastern North America</i>	3.77	0.34	0.67	0.22	0.64			0.18
<i>Central North America</i>	4.95*	0.48	0.67	0.16	0.87			0.15
<i>Western North America</i>	5.39	0.29	0.94	0.29	0.97			0.18
<i>Central America</i>	3.12*	-0.14	0.53	0.17	0.51			0.07
<i>Southern South America</i>	3.71	0.27	0.62	0.25	0.57			0.10
<i>Amazon Basin</i>	3.71*	0.01	0.63*	0.22	0.57*			0.07
<i>Southern Australia</i>	3.43*	-0.19	0.54	0.21	0.55			0.07
<i>Northern Australia</i>	3.42*	0.15	0.39	0.23	0.58			0.13

Precipitation (Yu2015) Results

Figure 20 has the precipitation regional changes. The largest positive changes occur in Southeast Asia, South Asia, Alaska, Eastern Africa, and Greenland. These changes are between 0.4 mm/day and 0.6 mm/day. The largest negative changes occur in

Central America, the Amazon Basin, and the Mediterranean Basin. These negative values range from -0.6 to -0.4 *mm/day*. The global regional average precipitation change is about 0.2 *mm/day* and is significant. This is as expected as increasing global temperatures increases evaporation and precipitation.

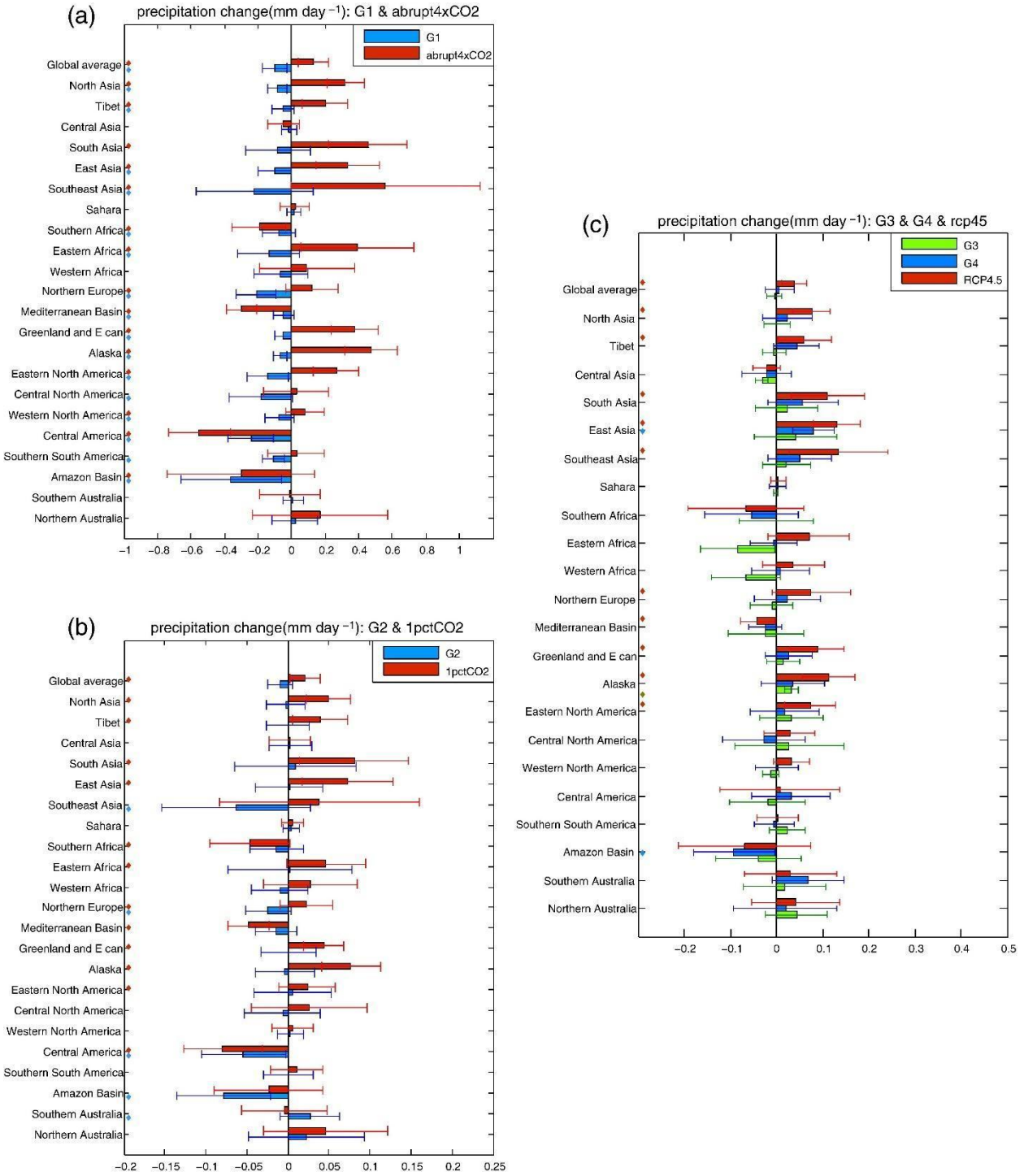
For G1 – piControl, the global regional average precipitation change is significant and has a value of about -0.2 *mm/day*. It seems that increased radiative forcing increases precipitation while decreasing radiative forcing decreases precipitation. All significant changes are negative with the largest negative changes occurring in the Amazon Basin, Central America, Southeast Asia, and Northern Europe. These precipitation changes range in value from about -0.4 *mm/day* to -0.2 *mm/day*.

For 1pctCO₂ – piControl, the global regional average is significant and has a value of about 0.05 *mm/day* which is significantly less than the change for Abrupt 4xCO₂ – piControl. The largest positive changes occur in South Asia, Alaska, and East Asia. These changes are all around 0.1 *mm/day*. The largest negative changes occur in Central America, Mediterranean Basin, and Southern Africa and have a change between about -0.1 and -0.05 *mm/day*. For the G2 – piControl experiment, the global regional average change in precipitation was insignificant. The only regions that had significant changes were Southeast Asia, Northern Europe, Central America, Amazon Basin, and Southern Australia. These were all negative and had values ranging from -0.1 and -0.05 *mm/day*.

The RCP4.5_2030_2069 – RCP4.5_2010_2029 experiments have a significant global precipitation increase of a little less than 0.1 *mm/day*. The largest positive changes occur in South Asia, East Asia, Southeast Asia, and Alaska with values all around 0.1 *mm/day*. There were no significant negative changes in precipitation. For G3 –

RCP4.5_2010_2029, the only significant change is in Alaska. This precipitation change has a value of about 0.05 mm/day . Similarly, the only significant change for G4 – RCP4.5_2010_2029 is East Asia with a value of about 0.1 mm/day .

Figure 20: Regional precipitation changes where a diamond indicates whether the change passed a t test (Yu et al., 2015). The red bars indicate values for the increased CO₂ concentration scenarios while green and blue indicate the geoengineering experiments. Figure (a) and figure (b) correspond to reference scenario piControl and Figure (c) corresponds to reference scenario RCP4.5_2010_2029 (Yu et al., 2015).



Precipitation (NCAR) Results

Figure 21 and Table 11 show the regional precipitation results where Figure 21 gives a visual for regional change comparison while Table 10 contains exact values. The precipitation regional changes for Abrupt 4xCO₂ – piControl and G1 – piControl are insignificant although the value for Abrupt 4xCO₂ – piControl was close to the value from the Yu2015 results. The largest positive precipitation change occurs in Southeast Asia, East Alaska, and East Asia with respective values of 0.60, 0.38, and 0.34 *mm/day*. The largest negative change occurs in Central America with a value of -0.79 *mm/day*. The positive temperature changes are close to the values from Yu2015. Central America has the largest negative change of all the regions in Yu2015 and in the NCAR data although the change is greatest for the NCAR data.

For G1 – piControl, the global regional average precipitation change was insignificant. All significant changes are negative with the largest negative changes occurring in Central America, the Amazon Basin, Eastern Africa, Southeast Asia, Eastern North America, and Northern Europe. These precipitation changes were within the same range as the Yu2015 results and had the same top regions although their relative order was different.

The global regional average precipitation changes are insignificant for both experiments 1pctCO₂ – piControl and G2 – piControl. The only regional changes that are significant for 1pctCO₂ – piControl is North Asia. Central North America, Southeast Asia, Southern Australia, and East Asia had the largest positive change with values a little less than 0.1 *mm/day* while the largest negative change occurred in Central America with a value of -0.1 *mm/day*. The only values that are consistent with the Yu2015 results

are Alaska, East Asia, and Central America. For G2 – piControl, the only significant change occurred in Central America with a value of -0.15 mm/day . This is consistent with the results from Yu2015.

The global regional average is insignificant for both RCP4.5_2030_2069 – RCP4.5_2010_2029 and G3S – RCP4.5_2010_2029. The only significant precipitation change occurs for RCP4.5_2030_2069 – RCP4.5_2010_2029 in North Asia. The largest positive precipitation changes occur in East Asia, Southeast Asia, Alaska, Eastern North America, and the Amazon Basin while the largest negative precipitation changes occur in Central America. In the Yu2015 results there were no negative precipitation changes, and the positive changes have regional overlap with East Asia, Southeast Asia, and Alaska. For G3S – RCP4.5_2010_2029, there are no significant precipitation changes. Central America has the only precipitation change that is not very close to 0 with a value of -0.06 mm/day .

Both the Yu2015 and NCAR data found a decrease in precipitation in Central America and increased precipitation in East Asia and Southeast Asia for all scenarios. Many of the precipitation changes were close to 0 and did not pass the t test. The results for precipitation are also less consistent with the paper results than the SAT values are. The precipitation model results are likely not very accurate. The most consistent result is the large decrease in precipitation in Central America. This occurs to some degree across all scenarios although it is not a significant change for anything except G1 and Abrupt 4xCO₂. The Yu2015 results for G1, G2, Abrupt 4xCO₂, and 1pctCO₂ indicate a drought in Central America also although it is not observed for the RCP4.5_2030_2069, G3, or G4 scenarios.

Figure 21: NCAR Results for regional precipitation. Figure (a) is Abrupt 4xCO₂ - piControl and G1 - piControl. Figure (b) is 1pctCO₂ - piControl and G2 - piControl. Figure (c) is RCP4.5_2030_2069 - RCP4.5_2010_2029 and G3S - RCP4.5_2010_2029. The black dots indicate that the regions passed a t test and the change is significant. The purple dots indicate that the change was not significant.

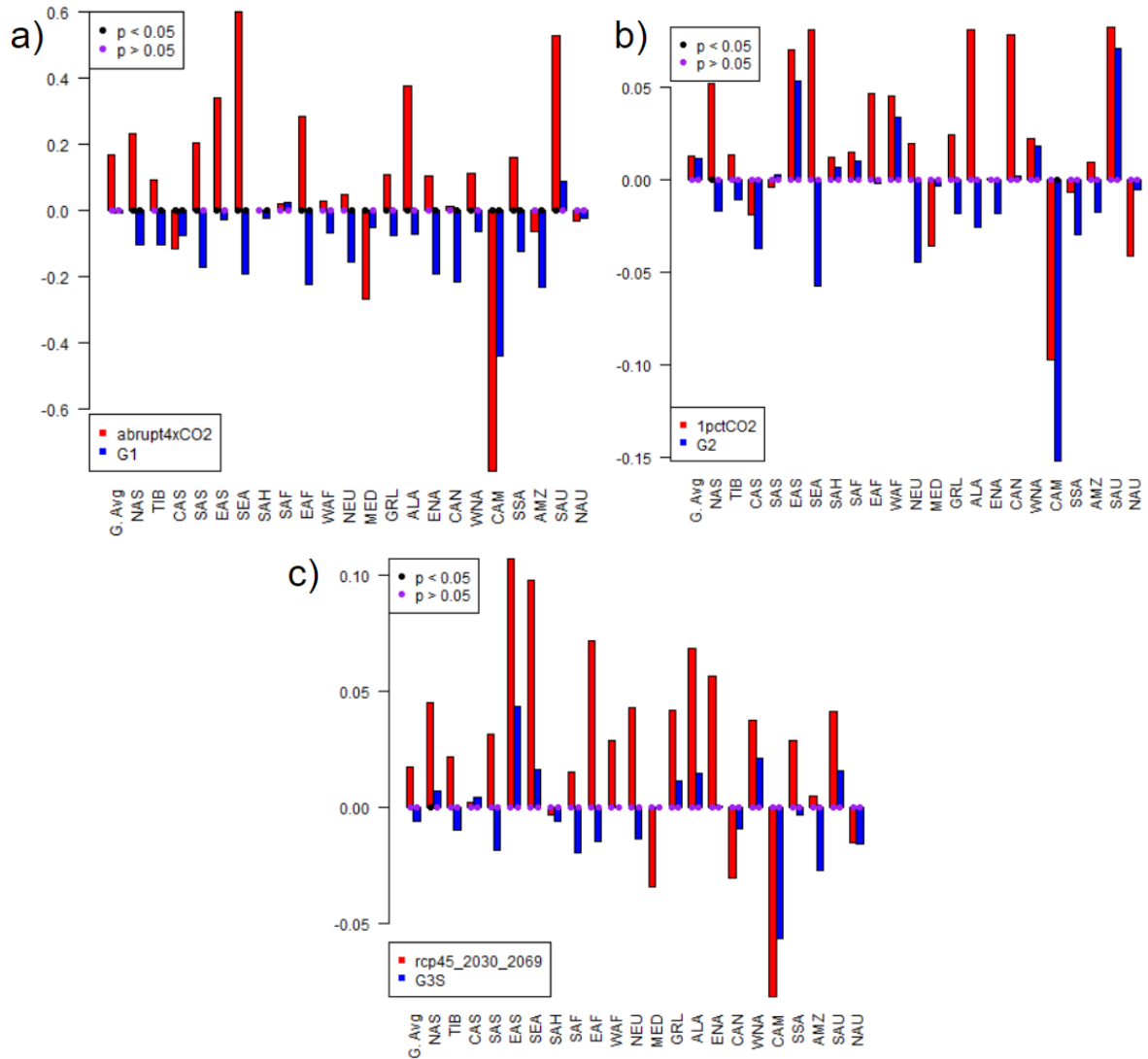


Table 11: Regional precipitation changes. The reference climate for the first 4 scenarios is piControl and for the last two it is RCP4.5_2010_2029. A star (*) next to the value in the table indicates that it passed the t test.

<i>Region</i>	<i>Abrupt 4xCO₂</i>	<i>GI</i>	<i>1pctCO₂</i>	<i>G2</i>	<i>RCP4.5_2030_2069</i>	<i>G3S</i>
<i>Global Average</i>	0.17	-0.01	0.01	0.01	0.02	-0.006
<i>North Asia</i>	0.23*	-0.11*	0.05*	-0.02	0.05*	0.007
<i>Tibet</i>	0.09	-0.11*	0.01	-0.01	0.02	-0.01
<i>Central Asia</i>	-0.12*	-0.07*	-0.02	-0.04	0.002	0.004
<i>South Asia</i>	0.20*	-0.17	-0.004	0.003	0.03	-0.02
<i>East Asia</i>	0.34*	-0.03	0.07	0.05	0.11	0.04
<i>Southeast Asia</i>	0.60*	-0.19*	0.08	-0.06	0.10	0.02
<i>Sahara</i>	-0.002	-0.02*	0.01	0.007	-0.004	-0.01
<i>Southern Africa</i>	0.02	0.03	0.01	0.01	0.01	-0.02
<i>Eastern Africa</i>	0.29*	-0.22*	0.05	-0.002	0.07	-0.01
<i>Western Africa</i>	0.028	-0.07	0.04	0.03	0.03	0.0005
<i>Northern Europe</i>	0.05	-0.16*	0.02	-0.04	0.04	-0.01
<i>Mediterranean Basin</i>	-0.27*	-0.05	-0.04	-0.003	-0.03	-0.0002
<i>Greenland</i>	0.11*	-0.08	0.02	-0.02	0.04	0.01
<i>Alaska</i>	0.38*	-0.07	0.08	-0.03	0.07	0.01
<i>Eastern North America</i>	0.10	-0.19*	0.001	-0.02	0.06	0.0007
<i>Central North America</i>	0.014	-0.21*	0.09	0.002	-0.03	-0.009
<i>Western North America</i>	0.11*	-0.07	0.02	0.02	0.04	0.02
<i>Central America</i>	-0.79*	-0.44*	-0.10	-0.15*	-0.08	-0.06
<i>Southern South America</i>	0.16*	-0.13*	-0.01	-0.03	0.03	-0.003
<i>Amazon Basin</i>	-0.06	-0.23*	0.01	-0.02	0.005	-0.03
<i>Southern Australia</i>	0.53*	0.09	0.08	0.07	0.04	0.02
<i>Northern Australia</i>	-0.03	-0.02	-0.04	-0.006	-0.02	-0.02

Summary

For the SAT changes, the largest positive temperature changes occur in Alaska, Greenland, North Asia, and Northern Europe. This remained true for the G1, G2, G3S, G3, and G4 scenarios although these scenarios still reduced the changes in these areas. These regions are all in the Northern Hemisphere at higher latitudes which was indicated by the volcanic research to have a greater climate variability from aerosol injection. Additionally, the paper attributes the pattern of increased warming near the poles and decreased warming near the equator as the result of the net effect between longwave greenhouse gas forcing and shortwave forcing which varies with the season and latitude (Yu et al., 2015).

Both the Yu2015 and NCAR data found that for all scenarios there is a decrease in precipitation in Central America and an increase in precipitation in East Asia and Southeast Asia. The results for precipitation are also less consistent with the paper results than the SAT values are. There was a large decrease in precipitation in Central America that was consistent across experiments. This is not observed for the RCP4.5_2030_2069, G3, or G4 scenarios which indicates that geoengineering could be successful in its prevention.

Section 3: Grid Level Map Outputs

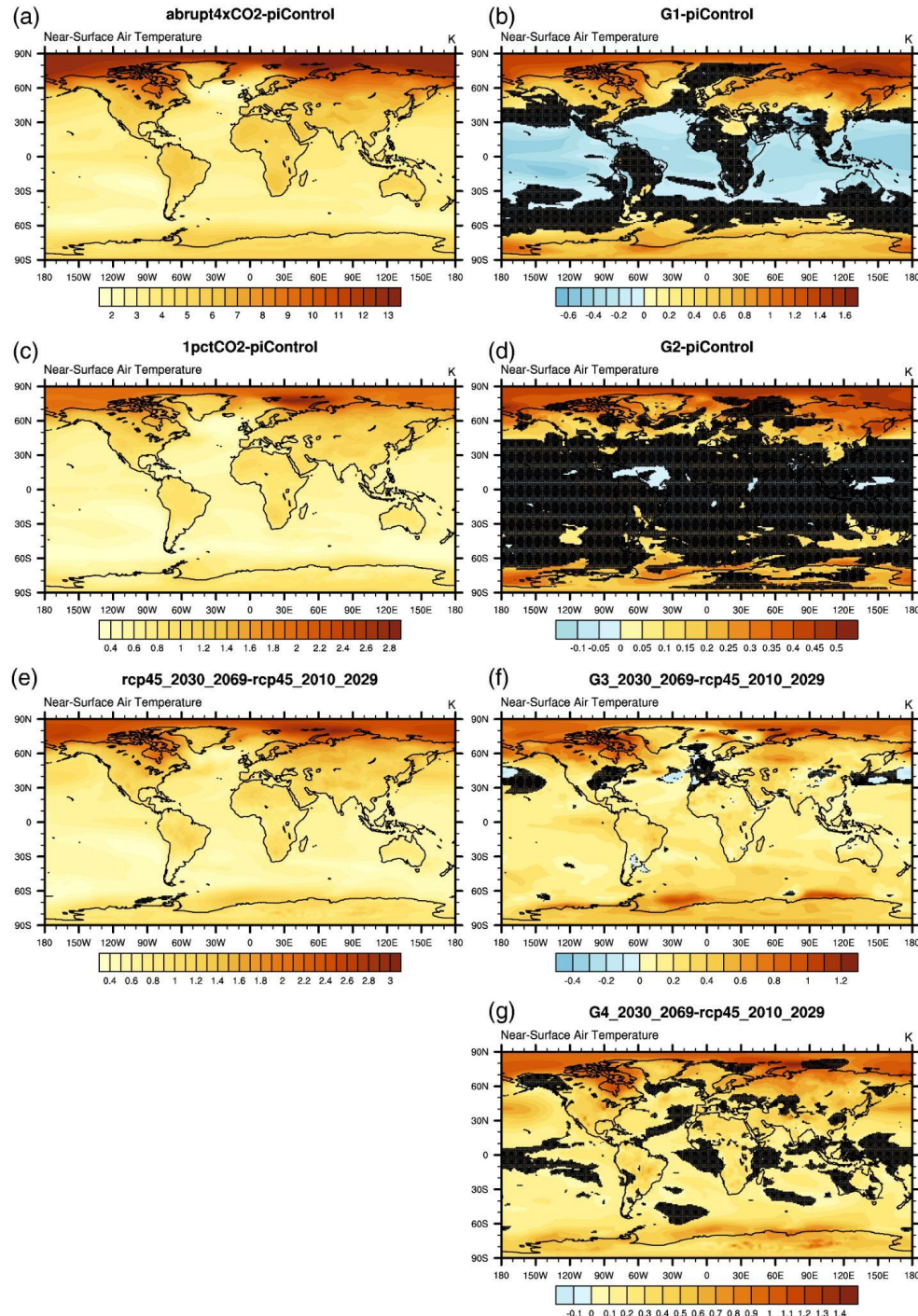
The maps in this section give the grid level change in SAT and precipitation. The results from the Yu2015 paper at the grid level are highly inconsistent between models, which makes comparison difficult and highlights the uncertainty in geoengineering

models at the smaller local level. For the NCAR data at the grid level the results are highly uncertain because the change is only based on a few data points. I obtained the regional data using the averages of the grid level inputs as well as the ensembles. The grid level results are only produced off of ensemble and time averages, which gives them a higher uncertainty.

Surface Air Temperature (Yu2015) Results

Figure 22 shows the results from Yu2015. The highest SAT change occurs at the North Pole for all models. For Abrupt 4xCO₂ – piControl, the North Pole has a temperature change of 13 °C and the coolest areas are the oceans which warm by about 2 °C. The SAT change at the North Pole for G1 – piControl drops to around 1.6 °C while the oceans cool by between -0.2 °C and -0.6 °C. For 1pctCO2 – piControl, the SAT drops by 2.8 °C at the North Pole and the oceans warm by between 0.4 °C and 0.6 °C. For G2 – piControl, the only location on the graph where the models agree is the North and South Poles which warm by only around 0.5 °C. For RCP4.5_2030_2069 - RCP4.5_2010_2029, the North Pole warms by 3 °C and the oceans are again between 0.4 °C and 0.6 °C. The model agreement for G3 – RCP4.5_2010_2029 is better than for G1 and G2. The North Pole warms by around 1.2 °C while the oceans warm by between 0 °C and 0.2 °C. There appears to be some cooling in Europe. Finally, G4 – RCP4.5_2010_2029 warms by 1.4 °C at the North Pole while the oceans are between 0.1 °C and 0.3 °C.

Figure 22: Ensemble mean of SAT anomalies results from Yu2015 for (a) G1 - piControl, (b) abrupt4xCO₂ - piControl, (c) G2 - piControl, (d) 1pctCO₂ - piControl, (e) G3 - rcp45_2010_2029, (f) G4 - rcp45_2010_2029, and (g) rcp45_2030_2069 - rcp45_2010_2029 (Yu et al., 2015). Stippling indicates areas where for G1 and Abrupt 4xCO₂ fewer than 10/13 models agreed on sign changes. This value is fewer than 9/12 for 1pctCO₂ - piControl, fewer than 2/3 models for G3 – RCP4.5_2010_2029, fewer than 6/8 models for rcp45_2030_2069 — rcp45_2010_2029, fewer than 2/3 models for G3 — rcp45_2010_2029, and fewer than 5/7 models for G4 (YU ET AL., 2015).



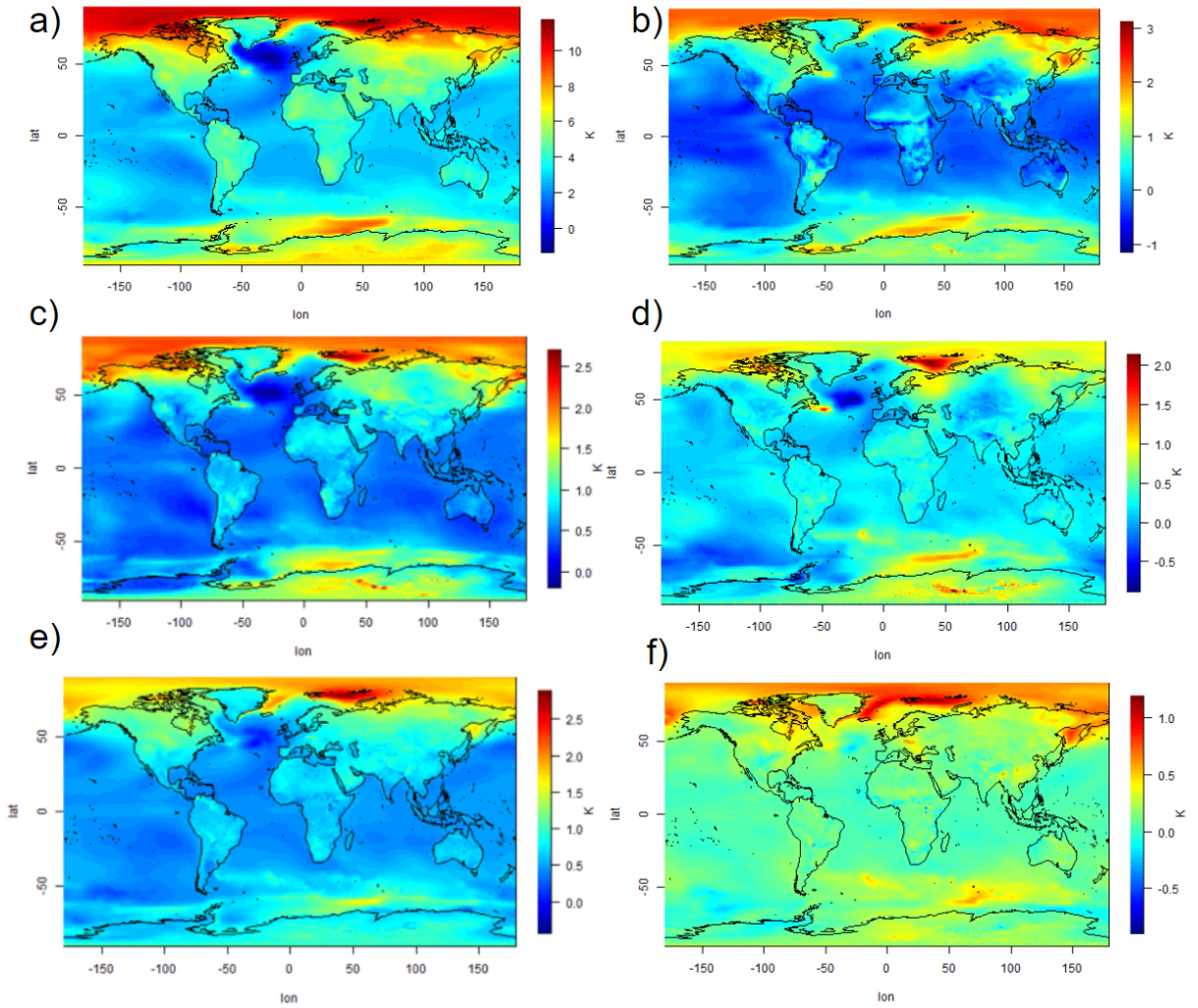
Surface Air Temperature Results (NCAR)

Figure 23 gives the results for the grid level changes for the NCAR data. The Abrupt 4xCO₂ – piControl has the same pattern as that of the Yu2015 results except that the North Pole only warms by around 10 °C and the oceans warm by between 2 °C and 4 °C. There is also a large patch below Greenland that appears to avoid any warming. For G1 – piControl, the North Pole warms by about 2 °C and the Equator cools by -1 °C. The North Pole values seem consistent with the result from Yu2015 while the oceans are cooling more in the NCAR data.

For 1pctCO₂ – piControl, the North Pole warms by between 2 °C and 2.5 °C and by 1 °C on the continents. The oceans appear cooler with little warming. This is consistent with the results from the Yu2015 paper. For G2 – piControl, the North Pole warms by between 1 °C and 2 °C and below 0.5 °C on the continents. Additionally, the spot below Greenland cools by -0.5 °C. The North Pole is consistent with the map from Yu2015 but the disagreement in the models makes it impossible to compare the continents with the NCAR data.

The North Pole for the RCP4.5_2030_2069 – RCP4.5_2010_2029 map warms by above 1.5 °C. The continents warm by 1 °C and the oceans by less than 0.5 °C. The extremity of the temperature change at the North Pole appears to be less for NCAR than for the Yu2015 results while the oceans and continent seems consistent. For G3S – RCP4.5_2010_2029, the North Pole warms by between 0.5 °C and 1 °C and by close to 0 on the continents and oceans.

Figure 23: Ensemble mean of NCAR SAT anomalies for (a) Abrupt4xCO₂ - piControl, (b) G1 - piControl, (c) 1pctCO₂ - piControl, (d) G2 - piControl, (e) rcp45_2030_2069 - rcp45_2010_2029, and (f) G3S - rcp45_2010_2029 (Yu et al., 2015). The temperature change gradient is given on the side of the map and is different for each scenario.

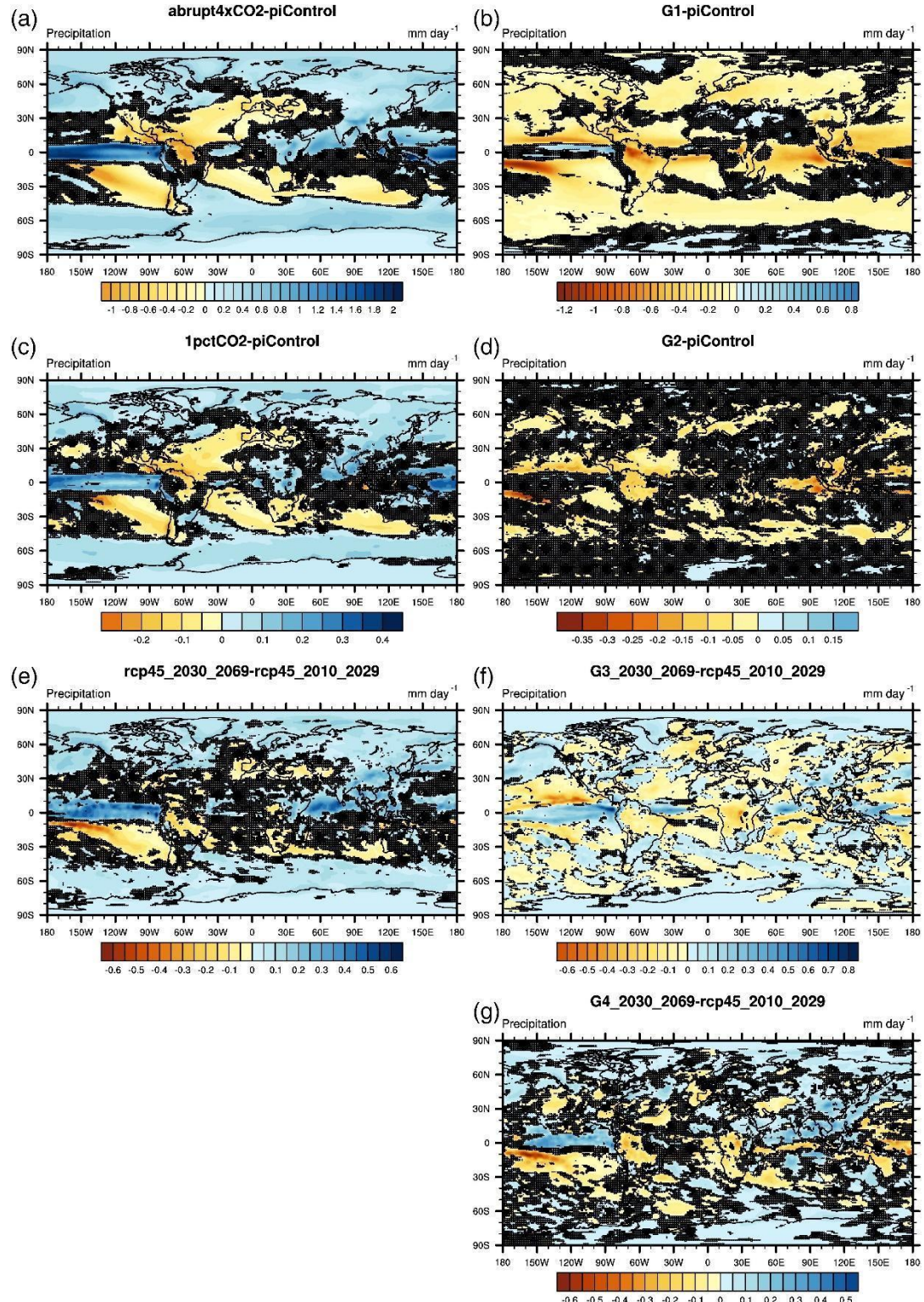


Precipitation (Yu2015) Results

Figure 24 shows the results from the Yu2015 paper and is similar to Figure 24 except for precipitation and not SAT. For Abrupt 4xCO₂ – piControl, locations with larger latitudes have a positive precipitation change while areas closer to the equator have a negative precipitation change. In G1 – piControl, the South Pole has an increase in precipitation while areas near the equator have a decrease. The rest of the area appears to

have a slight decrease in precipitation. Greenland has an increase in precipitation. For 1pctCO₂ – piControl, there is an increase in precipitation except near the equator. For G2 – piControl, the models do not agree on sign changes for most of the map. The G3 – RCP4.5_2010_2029 map has increased precipitation near the poles while the rest of the map alternates between increased and decreased precipitation. The models for the G4 map disagree on the sign change for most of the map.

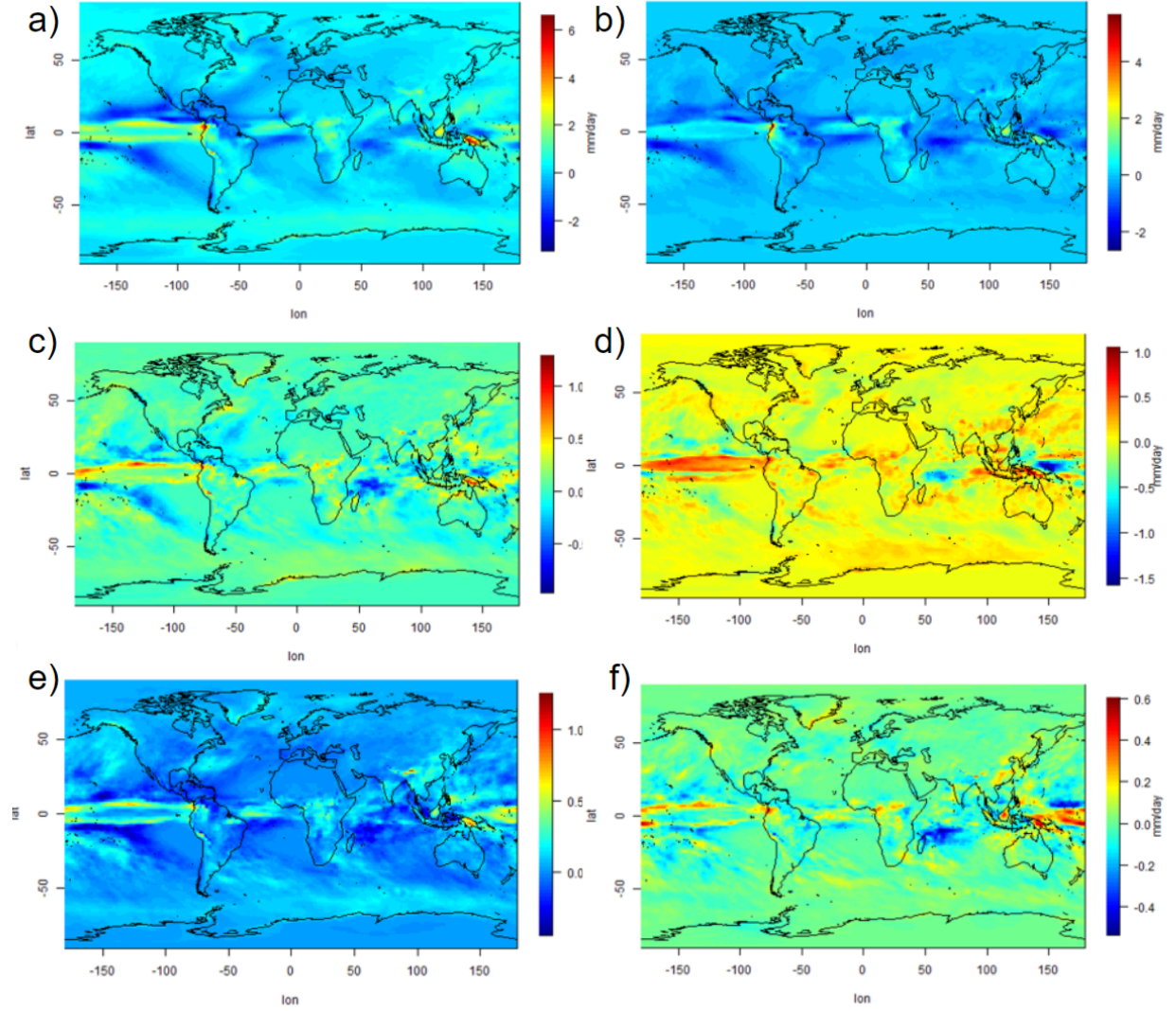
Figure 24: Ensemble mean of precipitation anomalies for G1 - piControl, abrupt4xCO₂ - piControl, G2 - piControl, 1pctCO₂ - piControl, G3 - rcp45_2010_2029, G4 - rcp45_2010_2029, and rcp45_2030_2069 - rcp45_2010_2029 (Yu et al., 2015).



Precipitation (NCAR) Results

Figure 25 shows the map for Abrupt 4xCO₂ – piControl, most of the precipitation change is slightly positive except at the equator, which has stripes of decreased precipitation. The map for G1 – piControl has a similar pattern except that most of the map has slightly negative precipitation except for the equator which has a close to -2 mm/day decrease in precipitation in some areas. For 1pctCO₂, there is no precipitation change for most of the area except for values by the equator, which are strips of decreased and increased precipitation. G2 – piControl has similar stripping but it extends further North and South than in the previous scenarios. For RCP4.5_2030_2069 – RCP4.5_2010_2029, there is a similar stripping pattern to the one observed in the previous scenario. The G3S – RCP4.5_2010_2029 scenario has dispersed areas of increased and decreased precipitation near the poles while the larger latitude areas have a precipitation change of around 0. The most extreme precipitation changes occur at the Equator with varying areas of increased and decreased precipitation. It is challenging to effectively compare results due to disagreement between models in the Yu2015 data. It appears that more extreme precipitation changes occur at the Equator in the Yu2015 results.

Figure 25: Ensemble mean of precipitation anomalies for G1 - piControl, abrupt4xCO₂ - piControl, G2 - piControl, 1pctCO₂ - piControl, G3 - rcp45_2010_2029, G4 - rcp45_2010_2029, and rcp45_2030_2069 - rcp45_2010_2029 (Yu et al., 2015).



Summary

For the SAT changes, the North Pole consistently exhibited the largest change while the oceans exhibited the smallest change. The most extreme precipitation changes occur at the Equator with strips of increased and decreased precipitation. It is challenging to effectively compare results between the Yu2015 data and NCAR and there are many inconsistencies between models in the Yu2015 data and the paper and the NCAR data.

Conclusion

I provide a list of the key findings for the comparison between the Yu2015 and NCAR data. (1) The global averages agreed for the Yu2015 and NCAR data. The agreement of the models for the global weighted average supports the theory of aerosol injection being effective in balancing increasing radiative forcing due to increased CO₂ concentrations. (2) I found that the geoengineering scenarios G3S, G3, and G4 are effective in counteracting increased radiative forcing for the continental land mass. However, these scenarios did not succeed in fully mitigating warming at the Poles. (3) Across all results, the largest temperature changes occur in Alaska, Greenland, North Asia, and Northern Europe. These regions are at high latitudes in the Northern Hemisphere and agreed with volcanic observation that found a greater decrease in temperature for regions in the Northern Hemisphere. (4) Some of the precipitation results indicated a large decrease in precipitation in Central America. However, this only passed the significance test for the G1 and G2 scenarios which are not intended to model realistic climate scenarios. The result is less obvious for the realistic climate change and geoengineering scenarios. (5) The global average and regional results for precipitation indicate that increasing radiative forcing increases precipitation while decreased radiative forcing decreases precipitation (6) Additionally, areas around the equator experience greater variability in precipitation changes.

Compared to the global average, there are more inconsistencies in the regional results between the Yu2015 and NCAR datasets. Although there are regions that consistently experience similar patterns between models and sources, the magnitudes are not consistent and the ranking of regions changed. This supports the claim that although

the overall physical effects of sulfate aerosols on the climate are understood, the predictive abilities on fairly large regional scales are not consistent across models. The temperature and precipitation grid level maps had even larger disagreement between models which further highlights the uncertainty.

In order to feasibly implement an aerosol injection strategy, more modeling accuracy must be achieved on the local level. Even though the models indicate that the strategy would be effective in counteracting increased radiative forcing and decrease temperature globally, the regional and local effects could be devastating and unpredictable. For instance, the models suggest that aerosol injection would be less effective in decreasing temperatures at the Poles. This strategy would not address rising seas levels due to melting ice caps. Additionally, aerosol injection does not address the issue of ocean acidification. Additionally, many models predicted a decrease in precipitation in regions like Central America which could be destructive to local inhabitants. It should also be noted that although precipitation effects were explored, other important climate variables were not analyzed. For instance, aerosols have been known to deplete the ozone layer which could have detrimental effects. Although the evidence supports aerosol injection as effective in counteracting increasing radiative forcing, inconsistencies in its local and regional climate effects make it an unrealistic strategy at present. Models and experiments done on atmospheric response would need to yield consistent results before the strategy could be seriously implemented.

Bibliography

- Bradley, R. S., & Jonest, P. D. (1993). 'Little Ice Age's summer temperature variations: their nature and relevance to recent global warming trends. *The Holocene*, 3(4), 367-376.
- Chin, M., & Kahn, R. (2009). *Atmospheric aerosol properties and climate impacts* (Vol. 2): US Climate Change Science Program.
- Christensen, J., Hewitson, B., Busuioc, A., Chen, A., Gao, X., Held, I., . . . Whetton, P. (2007). Regional Climate Projections. In.
- Giorgi, F., & Francisco, R. (2000). Evaluating uncertainties in the prediction of regional climate change. *Geophysical Research Letters*, 27(9), 1295-1298.
- Kravitz, B., Robock, A., Boucher, O., Schmidt, H., Taylor, K., Stenchikov, G., & Schulz, M. (2010). Specifications for GeoMIP experiments G1 through G4. URL: http://climate.envsci.rutgers.edu/GeoMIP/docs/specificationsG1_G4_v1.0.pdf [Accessed March 2015], Version, 1.
- Kravitz, B., Robock, A., Boucher, O., Schmidt, H., Taylor, K. E., Stenchikov, G., & Schulz, M. (2011). The geoengineering model intercomparison project (GeoMIP). *Atmospheric Science Letters*, 12(2), 162-167.
- Mann, M. E. (2002). Little ice age. *Encyclopedia of global environmental change*, 1, 504-509.
- Moreno-Cruz, J. B., Ricke, K. L., & Keith, D. W. (2012). A simple model to account for regional inequalities in the effectiveness of solar radiation management. *Climatic Change*, 110(3), 649-668.
- Robock, A. (2000). Volcanic eruptions and climate. *Reviews of geophysics*, 38(2), 191-219.
- Voiland, A. (2010). Aerosols: Tiny Particles, Big Impact. Retrieved from <https://earthobservatory.nasa.gov/features/Aerosols>
- Yu, X., Moore, J. C., Cui, X., Rinke, A., Ji, D., Kravitz, B., & Yoon, J.-H. (2015). Impacts, effectiveness and regional inequalities of the GeoMIP G1 to G4 solar radiation management scenarios. *Global and Planetary Change*, 129, 10-22.